Colloids and Surfaces A: Physicochemical and Engineering Aspects 687 (2024) 133476

Contents lists available at ScienceDirect

Colloids and Surfaces A: Physicochemical and Engineering Aspects

journal homepage: www.elsevier.com/locate/colsurfa

Zn induced surface modification of stable goethite nanoparticles for improved regenerative phosphate adsorption

C. Belloni [a,b,*], L. Korving [a], G.J. Witkamp [b,c], E. Brück [b], A.I. Dugulan [b]

[a] Wetsus, European Centre of Excellence for Sustainable Water Technology, Oostergoweg 9, Leeuwarden 8911 MA, the Netherlands
[b] Fundamental Aspects Mat & Energy Group, Delft University of Technology, Mekelweg 15, Delft 2629 JB, the Netherlands
[c] Water Desalination and Reuse Center, BESE Division, King Abdullah University of Science and Technology, Saudi Arabia

GRAPHICAL ABSTRACT

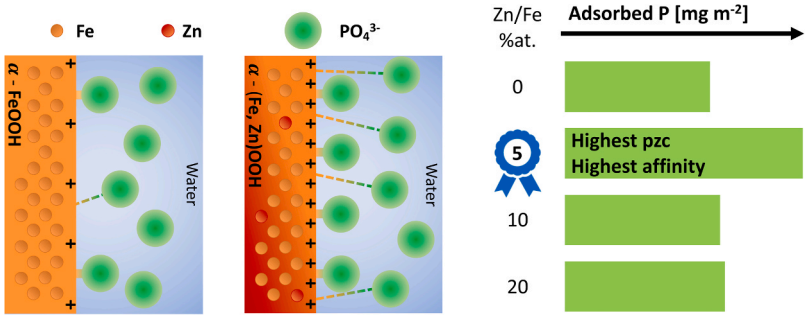

ARTICLE INFO

Keywords:
Phosphate recovery
Adsorption
Regeneration
Iron oxide
Goethite
Zinc doping

ABSTRACT

Iron oxide-based adsorbents showed potential to reach ultra-low phosphorus (P) concentrations to prevent eutrophication and recover P. High affinity, high capacity at low P concentrations (<1 mg L^{-1}), good stability, and reusability of the adsorbent are key factors for economic viability. In this study, nanoparticles of goethite (α-FeOOH), a highly stable phase, have been synthesized with increasing Zn^{2+}-doping, 0–20 %at. Zn/Fe, to manipulate the surface properties, following the results of a previous work. Mössbauer spectroscopy showed preserved goethite phase and increased point of zero charge (pzc) at low Zn-doping percentages, while at higher percentages (>5%at.) co-existing phases with increased specific surface area formed. Low concentrations (0.1–10 mg L^{-1}) batch adsorption tests showed increased P removal per unit mass with increasing doping. However, the highest pzc, affinity and P removal per unit area were observed for the 5%at. doped sample, suggesting this dopant concentration to provide the most effective surface. A regeneration test, performed at a lower pH than usual, showed preserved, even improved P desorption with increasing doping. Mössbauer spectroscopy showed that the nanoparticle phase and composition, up to 5%at., doping was preserved throughout the

Abbreviations: WWTP, Waste Water Treatment Plant; P, Phosphorus/Phosphate; NPs, Nanoparticles; HAIX, Hybrid Anion Exchange Adsorbent; M, Metal; MQ, Milli-Q Water; DW, Demineralized Water; ICP, Inductively Coupled Plasma Optical Emission Spectroscopy; TEM, Transmission Electron Microscopy; SAED, Selected Area Electron Diffraction; SSA, Specific Surface Area; Pzc, Point of Zero Charge; RMSPE, Root Mean Squared Percent Error; XRD, X-Ray Diffraction; MS, Mössbauer Spectroscopy; RT, Room Temperature; T_N, Néel Temperature; IS, Isomer Shift; QS, Quadrupole Splitting; H_f, Hyperfine Field.

* Corresponding author at: Wetsus, European Centre of Excellence for Sustainable Water Technology, Oostergoweg 9, Leeuwarden 8911 MA, the Netherlands.
E-mail addresses: c.belloni-1@tudelft.nl, carlo.belloni@wetsus.nl (C. Belloni).

https://doi.org/10.1016/j.colsurfa.2024.133476
Received 8 November 2023; Received in revised form 30 January 2024; Accepted 12 February 2024
Available online 17 February 2024

process. These results are promising to develop a stable effective Zn-doped goethite-based adsorbent for P recovery at ultra-low concentrations.

1. Introduction

Phosphorus (P) recovery is fundamental for three main reasons. First, it is an irreplaceable and vital nutrient, essential to the world food production sustainability [1,2], and its demand will further increase due to population growth [3], having increased already by 7.0% between 2019 and 2021 [4] and predicted to increase by 50% or more by 2050 [5,6]. Second, P is a finite and non-renewable resource which comes from phosphate rock mines, with reserves available in only a few countries, with Morocco alone estimated to possess 70% of the world-wide reserves, making Europe almost completely dependent on its import [3,7,8]. This led the European Commission to include P in the Critical Raw Materials list [8], asking for a more circular nutrients and resources management [9,10]. Third, through agricultural runoff and wastewater treatment-plant (WWTP) effluents, P reaches surface water-bodies where it accumulates, becoming a pollutant [11–15]. P in water can be found both in particulate and solute state. The latter comprises phosphate, which is the bioavailable P fraction causing eutrophication, promoting algae bloom entailing several-related issues. Environmental damages, causing the death of aquatic life; health risk, as some algae are toxic; and socio-economic damages, estimated in million to billions of euros (up to 200 M€ in the UK and 2 G€ in the US) of losses in tourism, fishing activities, property value, and so on [16–19]. To prevent eutrophication, P concentrations in freshwater bodies need to be limited to ultra-low concentrations, below 0.02 mg L^{-1} [20], which is hundred times lower than current regulations for WWTP effluents (< 1–2 mg L^{-1}) [21]. Moreover, the Water Framework Directive (WFD) [1] requires all European surface waters to reach a good ecological status by 2027, and the latest report from 2018 of the European Environment Agency highlighted that still 60% of the surface waters failed to meet this requirement [22]. This could result in high fines if European countries do not comply with the WFD by 2027. Therefore, it is important to remove P from water, as well as to recover it to be reused. Physical, biological and chemical methods have been widely investigated for P removal, but few of them display potential for P recovery, even less when targeting ultra-low P concentrations [23].

Among the chemical P recovery methods, adsorption showed promising results at concentrations below 1 mg L^{-1}, especially to target the ultra-low P concentrations and to recover P, since the process can be reversed [23–25]. This makes reversible P adsorption a promising technique as a water polishing step, especially in the context of eutrophication prevention and the WFD [23]. A lot of work has been done on adsorption, often under laboratory conditions and either with single use or with expensive and sophisticated adsorbents [26–29], mainly focusing on the ("maximum) adsorption capacity. However, at the ultra-low P concentrations of interest, affinity is the key parameter, since it describes how good the adsorbent is in removing P even when there is little of it left in water (a sort of adsorbent capacity at the low concentrations [30]). It was shown that there is no correlation between the adsorption capacities and affinities of adsorbents reported in literature [30]. Moreover, little efforts have been spent on P-recovery and adsorbent regeneration, the latter being a key factor to make the P-removal process economically viable. Studies showed that reusing the adsorbent 50–100 times, would make the process economically convenient [23, 31].

In this regard, iron oxide-based adsorbents constitute a promising option, being cheap due to their high abundance, and showing good properties for P removal, such as good affinity and selectivity [30–35]. Also, by means of an alkaline wash they allow the recovery of P and the regeneration of the adsorbent, allowing for further reuse of the adsorbent, but also of the regeneration solution itself, by recovering P from it [24,25,31,33,35–37]. There are several commercially available iron oxide-based adsorbents but the mainly employed ones are porous granular adsorbents and hybrid anion exchange adsorbents (HAIX) [23, 24]. The former type, usually industrial by-products, is cheaper, relatively stable, and good performing thanks to their high specific surface area (SSA). However, this high SSA mainly comes from micropores, in which diffusion is very slow, resulting in slow kinetics [23]. The latter type is a more expensive engineered adsorbent, consisting of iron oxide nanoparticles (NPs) embedded in macroporous resin beads, and showed good P removal performances and faster kinetics [23]. However, Kumar et al., 2018 [24], observed a consistent phase transformation of the iron oxide NPs already after few P adsorption/desorption cycles, which highly lowered the performances. In fact, these NPs mainly consist of ferrihydrite, an amorphous and highly reactive species, which offers high SSA and hence high capacity. Nevertheless, ferrihydrite is also the most unstable iron oxide species, likely to transform over a wide pH range [32] into more stable and less reactive phases, such as goethite and hematite [24,32,38].

Goethite (α-FeOOH) is one of the most abundant and most stable phases, which showed good affinity for phosphate [39–46]. On the one hand, the stability of goethite makes it an interesting candidate from the regeneration point of view, implying a longer lifespan of the adsorbent. On the other hand, it might limit its reactivity, and thus its P adsorption potential. Many studies suggested ferrihydrite as a promising adsorbent for P recovery, due to its high capacity. Nevertheless, these studies were often performed at P concentrations 50–100 times higher than those of WWTP effluents and surface water bodies, giving little insight into the potential for application, and often neglecting ferrihydrite affinity for P. In this regard, Wang et al., 2013 [47], in their comparison study between ferrihydrite, goethite and hematite P removal performances, suggested ferrihydrite to be the most promising species, mainly based on its high capacity. In fact, they showed that ferrihydrite had the highest P removal per mass capacity, more than 10 and 20 times higher than that of goethite and hematite, respectively. However, at P equilibrium concentrations below ~ 77 mg L^{-1}, goethite showed significantly higher P removal compared to the others. This is also supported by its higher estimated affinity, about 10 and 20 times higher than that of hematite and ferrihydrite, respectively. Moreover, ferrihydrite dissolution was observed throughout the experiments. These results support the ideas that goethite is the most promising species for targeting the ultra-low P concentrations of interest, and that using adsorption capacity at high P concentrations is a misleading parameter, as previously pointed out by Kumar et al., 2019 [23]. Nevertheless, improving goethite properties for P adsorption would be beneficial.

In this perspective, the current work aims at developing an efficient goethite-based adsorbent. To exploit goethite stability while increasing its P recovery performances, doping constitutes a promising option. Doping is a technique widely employed in semiconductors [48–50] and catalysis [51–54], in which an elemental metal (M) impurity, i.e., the dopant, is introduced in a hosting material to alter its properties. Doping has often been erroneously referred to when dealing with coating, assembling, loading or impregnation of metal and/or NPs in composite materials [37,55–59]. Pure and M-substituted goethite has been widely investigated, both as naturally occurring goethite rock or as synthetic goethite [32,60–63]. The effects of impurities in goethite, mainly Al [64–76] and Mn [77–81], have been investigated for many different applications, some including phosphate, arsenate, and divalent cations removal alone. Zn-for-Fe substitution in goethite has been investigated mainly from the crystallization point of view [63,82], and it has been proposed to promote goethite protonation as a charge compensation mechanism [63], and zinc ferrite precipitation above ~10%at.

substitution [82]. However, the effect of Zn-doping on surface charge and its application to P adsorption/desorption have never been investigated before. A previous work form our research group [83] showed Zn-doped goethite to be promising for the proposed application, improving surface properties and adsorption performances. The current study aims at systematically investigating the effect of increasing doping on the goethite properties and P adsorption/desorption performances.

In this context, a fine characterization and intrinsic properties of the doped goethite samples has been obtained using Mössbauer spectroscopy (MS) as the main characterization technique. MS is a high-resolution nuclear gamma-ray based technique mainly used to investigate Fe-based materials, providing information on the sample properties from the "Fe-nuclei point of view". Employed as a fingerprint technique, it is possible to retrieve mainly three parameters from the spectral analysis: the isomer shift (IS), which provides information such as the oxidation state and character of ligands of Fe atoms; the quadrupole splitting (QS), which provides further information on the oxidation state as well as the charge distribution asymmetry around the Fe nuclei; and the hyperfine magnetic field (H_f), which provides information on the magnetic ordering of the sample. MS offers very high-resolution spectral features, and compared to other techniques, such as XRD, it has the advantage to be sensitive even to very fine and amorphous NPs and to be more specific in Fe phase identification and quantitative speciation. Especially when performing measurements at different temperatures, since low temperatures are necessary to obtain the Zeeman split in the Mössbauer spectra, allowing the identification of (super)paramagnetic phases [60]. Previous work in our group showed how MS could provide a more thorough phase identification and detect phase transformation of iron oxide-based adsorbents, with respect to other studies in literature [24,84]. Moreover, MS can help in confirming a successful and homogeneous M-for-Fe substitution in doped samples, while providing information on the effect of the dopants on the structural, chemical and magnetic properties [69,70,78]. This work stresses the importance of applying MS to Fe-based materials development and stability monitoring.

This study presents an investigation on the effect of increasing Zn-for-Fe substitution in goethite NPs, and its influence on the surface charge and the P adsorption/desorption performances, enabling the development of a stable and high performing Zn-doped goethite-based adsorbent for P recovery.

2. Experimental materials & methods

2.1. Chemicals

Potassium dihydrogen phosphate (KH_2PO_4), sodium chloride (NaCl), 1 M sodium hydroxide (NaOH), 1 M hydrochloric acid and 37% hydrochloric acid (HCl) were purchased at VWR (The Netherlands). 3-(N-morpholino) propane sulfonic acid (MOPS) and iron nitrate nonahydrate ($Fe(NO_3)_3 \cdot 9\ H_2O$, $M_w = 404.00$ g mol^{-1}) were obtained from Sigma-Aldrich (The Netherlands), and zinc nitrate hexahydrate ($Zn(NO_3)_2 \cdot 6\ H_2O$, $M_w = 297.48$ g mol^{-1}) from Alfa Aesar (Germany).

2.2. Nanoparticles synthesis

The goethite NPs were synthesized adapting the procedure of Villacís-García et al., 2015 [39]. In short: CO_2-free Milli-Q (MQ) water was prepared by overnight N_2-bubbling, to eliminate CO_2. Then, 50 g of Fe $(NO_3)_3 \cdot 9\ H_2O$ was added to 825 g of the CO_2-free MQ. Meanwhile, 200 mL of 2.5 M NaOH CO_2-free solution was prepared. The NaOH solution was then injected in the Fe solution at a controlled flow of 1 mL min^{-1} through a peristaltic pump (Cole-Palmer, Masterflex L/S), to obtain consistent results, under N_2 bubbling and 250 rpm stirring. Once NaOH addition was completed, the solution, now at pH > 12, was let stirring for further 30 min. The solution was then placed in an oven at 60 °C for 48 h, occasionally shook for homogeneity, to age the ferrihydrite-based suspension into goethite. The phase transformation was visually confirmed by the suspension color change, from a dark brown to ochre.

For the doped goethite NPs, the same procedure was applied, with the difference of the Fe solution consisting of a mixture of Fe and Zn salts in the 5, 10 and 20%at. Zn/Fe ratio, for which the salts were weighed accordingly. In this case, after the aging, the color changed from dark brown to orange/dark red/purple, depending on the amount of Zn added.

Each synthesis provided around 8 g of NPs suspension. The NPs suspensions were then filtered via Buchner filtration, obtaining the so-called NPs cake, which was first thoroughly rinsed with MQ water, and then recovered, resuspended in Demineralized Water (DW) through thorough shaking and 10 min sonication at 40 kHz (Bandelin, Sonorex RM16UH). Then, the pH was adjusted to around 7 (pH of interest for the adsorption experiments) using HCl and NaOH. The NPs were let to settle, and the supernatant was removed and replaced by DW adjusted to pH 7, until the supernatant reached a conductivity below 0.1 μS cm^{-1}.

The synthesized samples are referred to as G for the pure goethite, and G[Zn5], G[Zn10] and G[Zn20] for the 5, 10, and 20%at. Zn/Fe doped goethite NPs and are shown in Figure S1.

2.3. Nanoparticles characterization

The NPs were characterized combining several methods, to obtain a complete description of their features and properties.

The NPs suspensions pH and conductivity were measured with a SevenExcellence pH/Cond meter S470, Mettler-Toledo.

The NPs mass concentration in solution was estimated by weighing oven-dried (60 °C) fixed volumes of the suspensions.

To confirm the Zn/Fe %at. in the doped goethite NPs samples, an aliquot of the suspension was centrifuged, to remove the supernatant, dissolved in HCl 37% acid solutions, and analyzed with a Perkin Elmer Optima 5300 DV Inductively Coupled Plasma Optical Emission Spectroscopy (referred to as ICP).

The morphology of the synthesized NPs was observed using a JOEL JEM1400-plus Transmission Electron Microscopy (TEM) with a TVIPS F416 camera operating at 120 kV. The images were analyzed with ImageJ software to estimate the size of the NPs. Selected Area Electron Diffraction (SAED) was also employed to qualitatively investigate the NPs crystallinity.

X-Ray Diffraction (XRD) measurements provided information on the speciation of the NPs, as well as their crystalline structure and crystallite size. XRD measurements were performed with a PANalytical X'Pert pro X-Ray diffractometer mounted in the Bragg-Brentano configuration with a Cu anode (0.4 mm×12 mm line focus, 45 KV, 40 mA). X-Ray scattered intensities were measured with a real-time multi strip (RTMS) detector (X'Celerator). The data were collected in the angle range $10° < 2\theta < 100°$ with a step size of 0.008° (2θ); total measuring times were 1 h for G and G[Zn5], 1.5 h for G[Zn10] and 2 h for G[Zn20]. A spinner was used as a sample holder, to homogenize the results and minimize artifacts, such as increased intensity due to NPs preferential orientation during sample preparation. XRD patterns were analyzed in fingerprinting mode using the PANalytical X'Pert software.

MS measurements provided the speciation of the NPs, identifying and quantifying the different phases, assessing the successful and homogeneous Zn-for-Fe substitution and its effects on the intrinsic properties of the NPs, and investigating the NPs stability after regeneration. Measurements were performed at three different temperatures, 300 K (room temperature, RT), 120 K (set-up thermalization with liquid N_2) and 4.2 K (liquid He temperature). Transmission ^{57}Fe MS spectra were collected with conventional constant acceleration or sinusoidal velocity spectrometers using a ^{57}Co (Rh) source and calibrated to α-Fe. The MS spectra were analyzed with Mosswin 4.0 software [85], to retrieve the different parameters, i.e., IS, QS and H_f, the line-width (Γ) [mm s^{-1}] and the spectral contribution [%].

The point of zero charge (pzc), defined as the pH at which the net surface charge of the adsorbent is neutral, is an indirect measurement of the surface charge of the adsorbent. The pzc was estimated using the salt addition method, adapted from Mahmood et al., 2011 [86], and Tan et al., 2008 [87]. In short, multiple 50 mL centrifuge tubes were prepared with 10 mL of 5 g L^{-1} NPs suspension adjusted at different initial pH in the range 5–10, using NaOH and HCl. The samples were let to equilibrate in a shaking incubator (150 rpm, 25 °C) for at least 5 days. Then, the initial pH values, pH_{in}, were recorded, followed by addition of 0.526 mL 2 M NaCl solution (final NaCl concentration of 0.1 M). The samples were again let to equilibrate in a shaking incubator for at least a week. The final pH values, pH_{fin}, were recorded and the $\Delta pH = pH_{fin} - pH_{in}$ calculated. Experiments were run in duplicates. Sample preparation and measurements took place in a glovebox with N_2 atmosphere, and all solutions and NPs suspension where N_2-bubbled for several hours prior use, to prevent pH fluctuations due to CO_2 exchange with the solutions. The NPs suspensions were also sonicated for 10 min before use. The pzc corresponds to the pH value at which $\Delta pH = 0$, i.e., the pH value at which the plot ΔpH vs pH_{in} crosses the x axis (pH_{in}). The pzc was determined with two different approaches. The first, by interpolating the whole data sets with a polynomial curve that could better represent the trend over a wide range of data. The second, by identifying the closest data at the opposite sides to the x axis and interpolating them with a linear function (most common method). pH measurements provided maximum pH fluctuations around ± 0.10 after pH adjustment (pH_{in}), and within ± 0.05 after pH equilibrations (pH_{fin}), while the pH meter (handheld PH 20, VWR, with GE 114 WD electrode) had an accuracy of ± 0.02. The root squared sum combinations of these contributions provided an uncertainty of ± 0.11, which has been rounded up to ± 0.15, to provide a larger range of confidence. The results have been discussed in relative terms, i.e., by comparing the results obtained for the different samples, rather than in absolute terms.

Micromeritics Tristar 3000 was used to estimate the specific surface area (SSA) of the NPs via Brunauer-Emmett-Teller analysis. The measurement was carried out by degassing about 100 mg of dried NPs overnight under N_2 atmosphere, followed by N_2 adsorption-desorption cycles, which can be related to the surface area of the material. The retrieved data were analyzed through non-local density functional theory model in the built-in software.

Note that for MB, XRD and SSA measurements, the sample preparation consisted of NPs centrifugation to remove the supernatant from the so-called NPs cake; oven-drying at 40–60 °C of the NPs cake; grinding the recovered NPs powder to be then placed in the respective sample holders.

2.4. Phosphate adsorption experiments

To perform P adsorption experiments, KH_2PO_4 salt was used as a source of phosphate and all concentrations are reported in terms of phosphorus concentrations. A 500 mg L^{-1} P stock solution in DW was prepared, from which different dilutions were obtained, with P concentrations of 0.1, 0.5, 0.75, 1, 2.5, 5, 7.5 and 10 mg L^{-1} as starting concentrations (C_{dil} [mg L^{-1}]). Adsorption experiments were performed in 100 mL P solutions, in duplicates plus blank, i.e., P solution without adsorbent as a control. To keep the pH constant during the adsorption experiments, 20 mM of MOPS was added as a pH buffer, which is known to be a non-complexing agent, unlikely to influence phosphate in solution [88], as observed from the blanks. The pH value was adjusted using NaOH and/or HCl around 7.2, which coincides with one of the buffering points of MOPS, and falls within the pH range 6–8, typical of WWTP effluents and surface waters. At this pH, the phosphate ions are evenly distributed as mono- and di-valent phosphate, $H_2PO_4^-$ and HPO_4^{2-}, respectively [23,25,37,89]. Meanwhile, a NPs suspension of 1 g L^{-1} was prepared and sonicated for 10 min to promote NPs dispersion, and the concentration verified by weighing oven-dried volumes. Then, 10 mL of the P dilutions (C_{dil}) samples were removed (and analyzed with ICP) and replaced with 10 mL of the NPs suspension for the adsorption samples (final adsorbent concentration of 0.1 g L^{-1}), and with 10 mL DW for the blank samples. The so-prepared blank samples provided the initial P concentrations, C_0 [mg L^{-1}], which was determined with ICP. These concentration values were also verified with ICP results of the original dilutions, C_{dil}[mg L^{-1}], accounting for the 10 mL NPs suspension/DW addition via the formula:

$$C_0^{calc} = C_{dil} \bullet \frac{0.09L}{0.10L}$$

This procedure was chosen for practical reasons. The samples were then placed in a shaking incubator at 25 °C, 150 rpm. Preparatory experiments showed that equilibrium was reached well within two days, in agreement with other studies [90–92]. Nevertheless, some samples were further analyzed after one week, as a further control, without showing any appreciable difference.

2.5. Desorption/regeneration experiments

A regeneration experiment was run with the aim of assessing the influence of doping on the ease of P desorption and NPs regeneration, and NPs stability. It is well known that metal oxide-based adsorbents can be easily regenerated via an alkaline wash, often using 0.1–1 M NaOH, i.e., pH 13–14 [23–25,36,37,55,93]. Usually, in studies with NPs, the adsorption samples are centrifuged to separate the NPs from the adsorption solution, and then redispersed and regenerated. However, centrifugation is known to promote irreversible agglomeration of the NPs, which might cause phosphate blocking, while redispersion of NPs can require long sonication which might alter the NPs. In this study, the desorption was therefore performed by increasing the pH directly in the P solution after the adsorption equilibrium was reached, with the following procedure. First, an adsorption experiment was run similarly to the isotherm experiments, again in duplicates plus blank. Samples of 100 mL P solution at 25 mg L^{-1}, with 20 mM MOPS and pH 7.2 were prepared. Meanwhile, a 3 g L^{-1} NPs suspension was prepared and sonicated for 10 min. Then, 10 mL of the P solutions were removed and analyzed with ICP and replaced by 10 mL of the NPs suspension solution for the adsorption samples (adsorbent concentration of 0.3 g L^{-1}), and by 10 mL of DW for the blanks. The samples were then placed in a shaking incubator at 25 °C, 150 rpm. After five days, to be sure equilibrium was reached, 5 mL of the suspension was collected and filtered for analysis and replaced with 5 mL of 1 M NaOH solution, which increased the pH to around 12.6. The regeneration pH was deliberately chosen to be low compared to the usual pH (as previously mentioned), to enhance the differences in desorption, as observed by Zhang et al., 2009 [94].

The samples were placed in a shaking incubator at 25 °C, 150 rpm, for one day. Then, the solutions were filtered and analyzed with the ICP. The adsorption/desorption samples were then centrifuged to recover the NPs, which were then oven dried and analyzed with Mössbauer spectroscopy.

2.6. Samples analysis

The elemental composition of the P-based solutions was analyzed with ICP (detection limit of interest: P = 20 μg L^{-1}; Fe = 5 μg L^{-1}; Zn = 1 μg L^{-1}). The initial concentrations, C_0 [mg L^{-1}], were obtained both from the ICP analysis of the blanks at the start and end of the experiments, and from calculations from the C_{dil} analysis, and always displayed a good agreement, well within the 3% error. The equilibrium concentrations, C_{eq} [mg L^{-1}], were obtained from the ICP analysis of the adsorption samples. Prior to analysis, the samples were filtered with a 25 nm pore size filters (MF-Millipore Membrane Filter, 0.025 μm pore size, Merck), with the help of a six channel NE-1600 syringe pump (New Era Pump Systems, Inc.). Since no appreciable difference in the ICP results was observed between filtered and unfiltered blank samples, it was

assumed that filtration had a negligible influence on the samples' elemental concentrations at these ranges. The amount of P adsorbed normalized to the mass of adsorbent, q [mg g^{-1}], was calculated through the equation:

$$q = \frac{C_0 - C_{eq}}{m_{NPs}} V \quad (1)$$

where m_{NPs} [g] is the mass of adsorbent and V [L] is the volume of the sample.

2.7. Data analysis

For the adsorption isotherm analysis, the data were analyzed by plotting q against C_{eq}, and fitting them with two adsorption isotherm models, the Langmuir [95] and the Freundlich [96] isotherm models.

The Langmuir isotherm is an ideal adsorption model developed for gas adsorption on solid phase. The model is based on monolayer adsorption on homogeneous adsorption sites without interaction between adsorbate molecules. The Langmuir isotherm equation is given by:

$$q = \frac{q_{max} K_L C_{eq}}{1 + K_L C_{eq}} \quad (2)$$

where q_{max} [mg g^{-1}], is the capacity, which is represented by the height of the plateau of the curve, and K_L [L mg^{-1}] is the Langmuir constant which is related to the affinity between the adsorbate and the adsorbent binding sites, represented by the steepness of the ascending portion of the curve.

The Freundlich isotherm, suited to describe adsorption on heterogeneous adsorption sites, is an empirical model, meaning that its constants do not have a physical meaning. The Freundlich isotherm equation is given by:

$$q = K_F {C_{eq}}^n \quad (3)$$

where K_F [(mg g^{-1})(mg L^{-1})$^{-n}$] is the Freundlich constant (or adsorption strength), which is related to the capacity of the adsorbent, and n is a dimensionless constant representing the adsorption intensity, related to the surface sites' heterogeneity.

The fitting results were interpreted in relative terms, rather than absolute terms, purely as a matter of comparison. In fact, given the two models' limitations, the fitting parameters values should be evaluated with care.

Finally, the data were normalized not only to the mass of adsorbent, but also to its SSA, to provide further information from two different criteria of comparison, and again fit with the Langmuir and Freundlich models.

The fitting was performed using Microsoft Excel Solver, minimizing the RMSPE (Root Mean Square Percentage Error) and the goodness provided the reported RMSPE.

For the desorption analysis, the mass of P adsorbed, $m_{P,ads}$ [mg], was calculated using:

$$m_{P,ads} = (C_0 - C_{eq})V \quad (4)$$

and the mass of P desorbed, $m_{P,des}$ [mg], using:

$$m_{P,des} = (C_{des} - C_{eq}')V \quad (5)$$

where V [L] is the volume of sample, C_{des} [mg L^{-1}] represents the P concentration after desorption, and C_{eq}' represents the equilibrium concentration after adsorption, corrected for the dilution due to sampling and NaOH addition. Then, the mass percentages of desorbed P have been calculated via:

$$\%mg \quad P \quad desorbed = \frac{m_{P,des}}{m_{P,ads}}\% \quad (6)$$

Finally, the P surface coverage percentage in the adsorption/desorption experiments (both of the adsorbed P after adsorption and the undesorbed P after regeneration) were calculated, considering a phosphate ionic radium of 238 pm [97].

3. Results and discussion

3.1. Nanoparticles characterization

3.1.1. Elemental analysis

ICP measurements of dissolved NPs (in HCl 37%) confirmed the nominal Zn/Fe %at. for all samples, as reported in the Table 1. The average error from the replicates' measurements was smaller than 1% and was considered underestimated. Hence, an excess error of 5% was assigned to all the resulting values, to have a wider range of confidence.

3.1.2. Specific surface area

From the BET analysis of the SSA measurements the following SSA trend was observed: G[Zn20] > G[Zn10] > G $\gtrsim$ G[Zn5], as visible in Table 1, with G[Zn10] and G[Zn20] having SSA respectively two and three times higher than G and G[Zn5]. In the case of G, the SSA is of the same order of magnitude of generally reported in literature for goethite NPs [32]. The highly doped samples, G[Zn10] and G[Zn20] respectively show two and three times the SSA compared to of G and G[Zn5]. This is in line with TEM observation (in the following section), which showed the presence of ultrafine NPs.

3.1.3. TEM

TEM imaging (Fig. 1) showed that the NPs in sample G have a rod-like shape, as expected [32], with a certain degree of size distribution. For the doped samples, it is visible that the length of these rods increases with increasing doping, while the opposite trend is observed for the width, insofar they look like filaments in the G[Zn20] images. While G[Zn5] appear to display one unique phase of elongated rod-shaped NPs, G[Zn10] and G[Zn20] display a coexistence of multiple phases, with the former presenting a moderate amorphous/fine NPs fraction, while the latter presenting a consistent amorphous/fine NPs fraction and few small spherical/cubic NPs. A clear particle size estimation from TEM images was not possible since the NPs clustered together during sample preparation. However, a rough estimation was obtained analyzing the images with ImageJ, by mean of a gaussian distribution of the measured values of more than 200 NPs per sample, and the values are reported in Table 2. For the rod-shaped NPs it is visible how, with increasing doping, the average length increased from 102 nm up to 185 nm for G[Zn10] (164 nm for G[Zn20]), while the average width decreased from 11 nm down to 6 nm. For the spherical/cubic NPs in sample G[Zn20], an average diameter of 13 nm was estimated. Further TEM investigation is recommended to better clarify the shape and structure of the NPs, and perhaps the elemental distribution via TEM-EDS.

3.1.4. X-ray diffraction

XRD patterns (Fig. 2) analyzed with PANalytical X'Pert software showed a good match of samples G, G[Zn5] and G[Zn10] with the goethite phase. Differences in peak intensities could be related to the preferential orientation of the rods, and difference in aspect ratio and

Table 1
Theoretical and experimental doping %at. from ICP analysis after NPs acid dissolution, and SSA values from BET analysis of the different synthesized NPs.

Sample	*Theoretical Zn/Fe %at.*	*Experimental Zn/Fe %at.*	*SSA [m^2 g^{-1}]*
G	0	0	84.7 ± 0.9
G[Zn5]	5	5.1 ± 0.3	76.0 ± 0.8
G[Zn10]	10	10.2 ± 0.5	165 ± 1
G[Zn20]	20	21 ± 1	231 ± 2

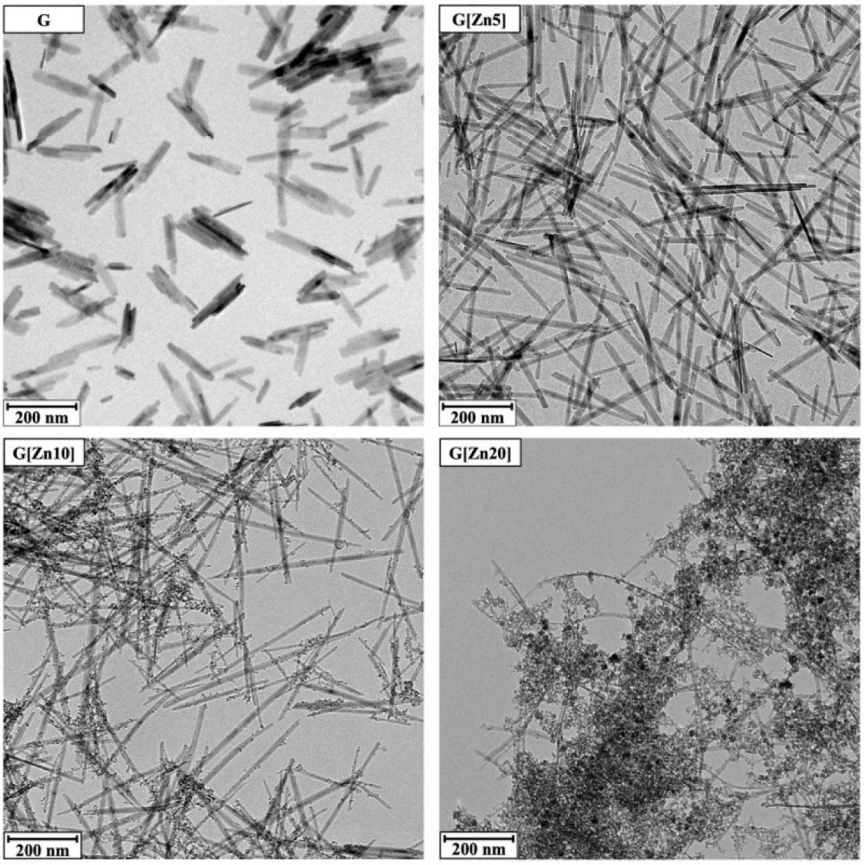

Fig. 1. TEM images of the synthesized NPs.

Table 2
Particle size estimation of the synthesized NPs from TEM images using ImageJ software.

Sample	*Rod-shaped NPs*						*Spherical /cubic NPs*			*Amorphous NPs*
	Length [nm]			*Width [nm]*			*Diameter / Side [nm]*			
	Min	*Max*	*Mean*	*Min*	*Max*	*Mean*	*Min*	*Max*	*Mean*	
G	11	305	102 ± 46	3	23	11 ± 3	-	-	-	-
G[Zn5]	12	330	115 ± 55	3	20	9 ± 3	-	-	-	-
G[Zn10]	25	468	185 ± 88	2	13	6 ± 2	-	-	-	Small amount
G[Zn20]	24	462	164 ± 77	1	13	6 ± 2	5	24	13 ± 4	Significant amount

crystallinity of the NPs, the latter also influencing the peak broadening. Sample G[Zn20] showed a good agreement with both the goethite and the zinc ferrite ($ZnFe_2O_4$) phases, with a semiquantitative estimation of 44% and 56%, respectively. This estimation provides an order of magnitude, rather than an absolute value. The formation of zinc ferrite with increasing Zn concentration is in agreement with the results of Krehula et al., 2006 [82] The increased peak broadening and noise in G [Zn10] and G[Zn20] can be attributed to reduced crystallinity of the NPs (as confirmed by SAED, see section S.2 in S. I.). It is challenging to confirm whether the amorphous/fine NPs observed with TEM contributed to the XRD signal, and thus to the phase identification. In this sense, MS becomes essential. Finally, an indicative estimation of the crystallite sizes (dominated by the NPs width, compared to the NPs size estimation in Table 2, in agreement with [98]) from the XRD patterns analysis is reported in Table 3.

3.2. Mössbauer spectroscopy

Mössbauer spectra are presented in Fig. 2 and the fitting parameters of interests, IS, QS, and H_f, together with Γ and the spectral contribution are reported in Table 4, where also the reference hyperfine values of bulk goethite [99] are reported. In general, MS results showed that Zn-doping < 10%at. provided single goethite phase NPs, while ≥ 10%at. showed multiple goethite and/or other phases were observed. Also, increasing doping increased the paramagnetic character of the NPs, due to Zn-for-Fe substitution, hence lowering the magnetic ordering temperatures of the different samples. A more detailed discussion for each sample is provided hereafter.

MS measurements of sample G were performed at RT and 120 K. The RT spectrum of G displays a sextet with asymmetrically broadened peaks typical of non-bulk goethite with particle size distribution and non-perfect crystallinity, in agreement with TEM, SAED and XRD results. The 120 K shows a sextet with sharper and more symmetrical lines, as expected since the internal magnetic field increases with decreasing temperature, as a consequence of reduced thermal excitations, which causes the magnetic spins to flip [99]. The spectral analysis provided IS and QS values typical of high-spin Fe^{3+} in octahedral coordination. The RT mean H_f = 32.4 T is close but smaller than that of bulk goethite (38.0 T), due to the nano-sized dimension of the particles, for which surface boundary effects attain higher importance, the particle size

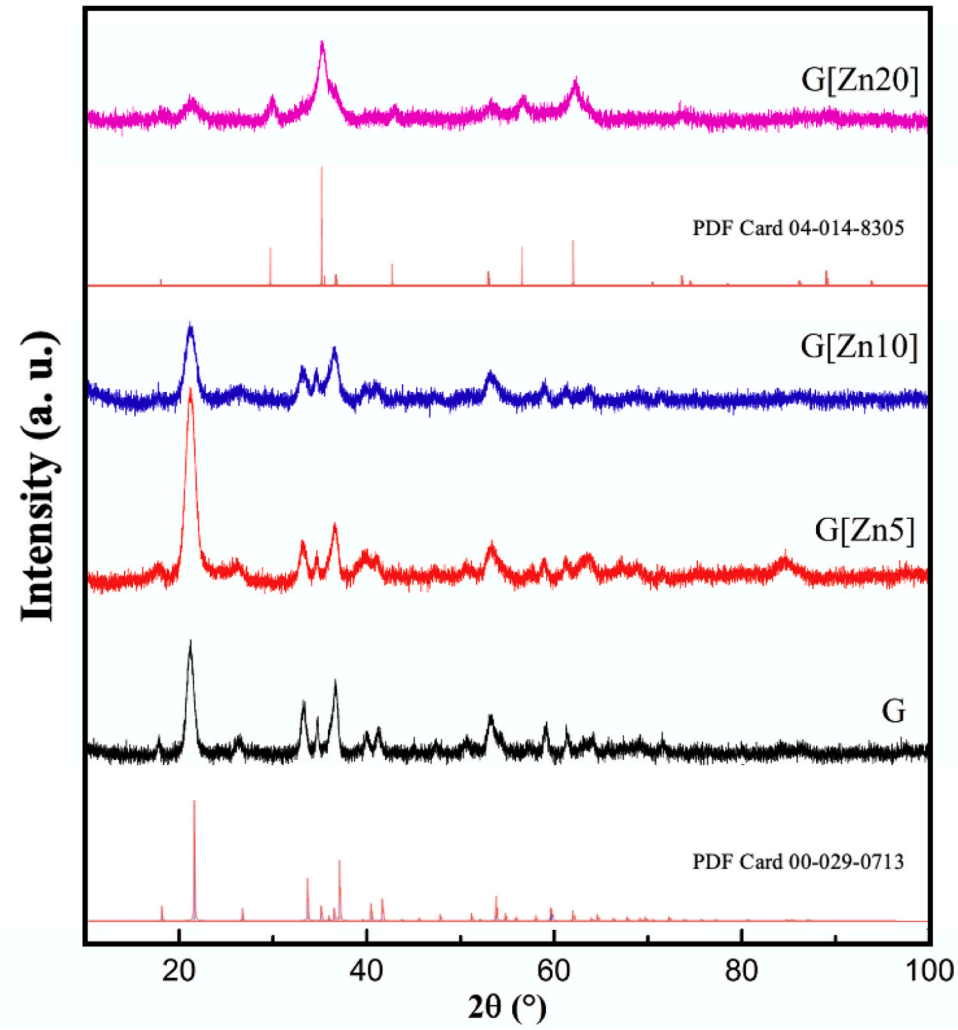

Fig. 2. XRD patterns of the synthesized NPs and the reference goethite pattern (PDF Card 00–029-0713) and zinc ferrite pattern (PDF Card 04–014-8305).

Table 3
Indicative estimation of the crystallite sizes from the measured XRD patterns of the synthesized NPs.

Sample	*α-FeOOH*	*$ZnFe_2O_4$*
G	120 Å	-
G[Zn5]	70 Å	-
G[Zn10]	60 Å	-
G[Zn20]	60 Å	170 Å

distribution in the sample and the non-perfect crystallinity. The 120 K mean H_f = 48.9 T is closer to the saturation value of bulk goethite (50.6 T), following the expected behavior of the hyperfine magnetic field with temperature [60]. Since no other spectral contributions are visible at this temperature, the spectrum was unambiguously attributed to pure polycrystalline goethite.

Sample G[Zn5] was analyzed at RT and 4.2 K, the latter temperature to investigate whether the Zn-for-Fe substitution was homogeneous or promoted multiple phases formation. Again, both spectra provided IS and QS values in agreement with high-spin Fe^{3+} in octahedral coordination and with those of G. The peak broadening in the RT spectrum of G[Zn5] are again related to the particle size distribution and non-perfect crystallinity, again in agreement with TEM, SAED, and XRD results. As expected from the diamagnetic Zn-for-Fe substitution (similarly to Al-doping [65,69,70]), there is a reduced magnetic coupling between the different Fe sites in the crystal, which entails mainly two effects. First, the decrease of the magnetic interaction between Fe sites, reducing the magnetic ordering temperature or Néel temperature (T_N), which for pure goethite is ~ 400 K. This is represented by the doublet feature, accounting for paramagnetic-like behavior. Second, the reduced magnetic hyperfine field supertransfer, which reduces the H_f value [99], now equal to 24.6 T, against 38.0 T of bulk goethite and 32.4 T of G. Considerations on particle size distribution and surface effects still hold. The 4.2 K spectrum displays one unique sextet with sharper peaks, proving the uniqueness of the phase and the successful and homogeneous Zn-for-Fe substitution. The mean H_f = 49.6 T is lower than the saturation value of bulk goethite (50.6 T), due to the presence of Zn (as previously discussed), in agreement with what was observed by Krehula et al., 2006 [82], and for Al-substitution by Murad et al., 1987 [69].

For the G[Zn10] sample, measurements at RT, 120 K and 4.2 K were carried out. It is possible to see that the increasing Zn-for-Fe substitution and the formation of an amorphous/fine NPs fraction (observed with TEM) increased the relaxation effects (see section S.3 in S. I.), causing the RT spectrum to collapse into a broad doublet. As temperature decreases, magnetic ordering takes place, until complete magnetic ordering is restored at 4.2 K, as visible by the sextet. The green spectral features present at RT and 120 K account for relaxation effects. For all the spectra, the IS and QS values fall within the high-spin Fe^{3+} in octahedral coordination range. In particular, the QS = 0.48 mm s^{-1} of the red doublet in the RT spectrum is in good agreement with that expected for paramagnetic goethite (0.48 mm s^{-1} [100–102]), while that of the blue doublet at RT and 120 K, 0.81 and 0.85 mm s^{-1} respectively,

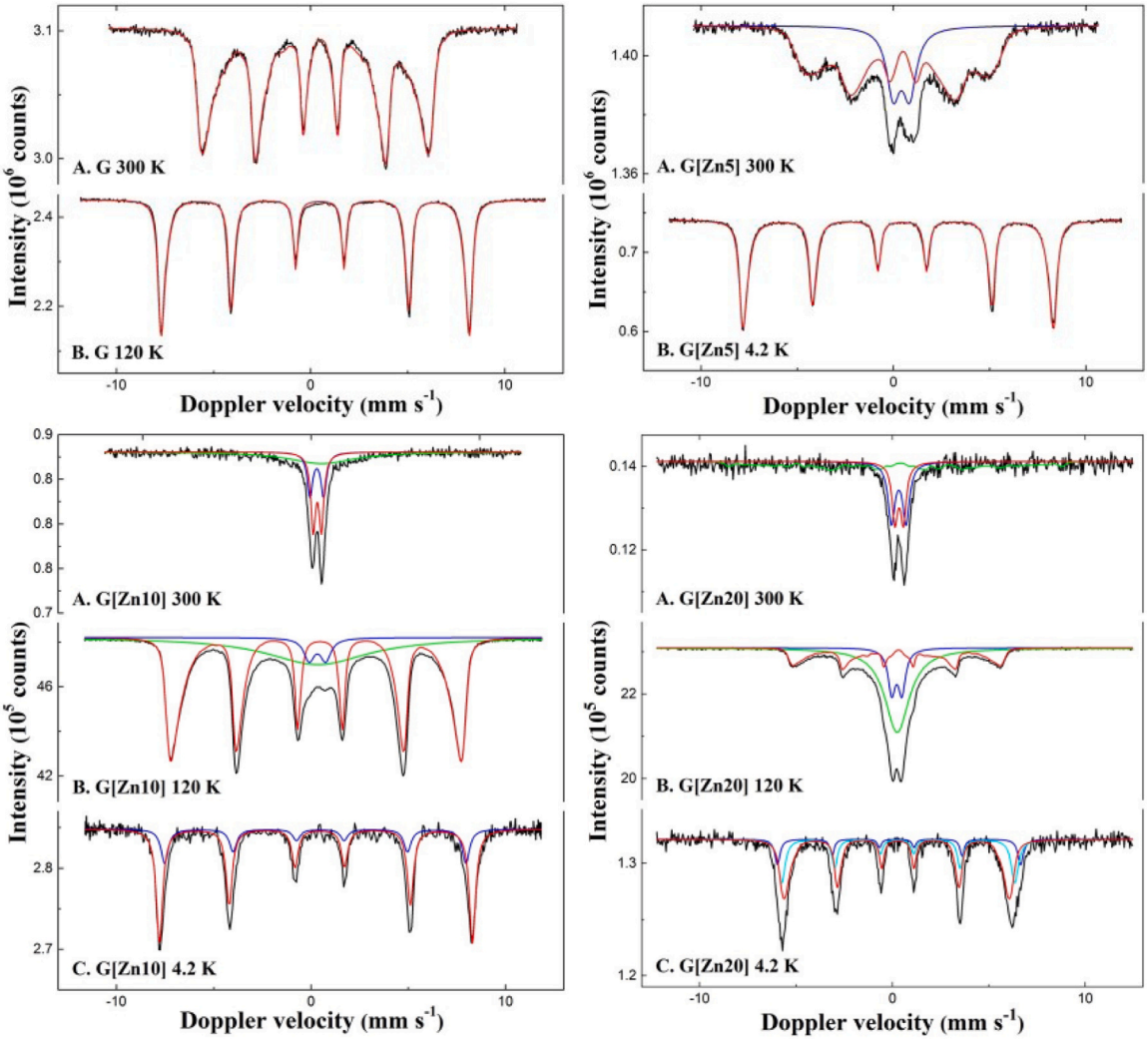

Fig. 3. MS spectra of the synthesized NPs measured at different temperatures (300, 120 and 4.2 K). Black lines represent the measured spectra, colored lines represent the fitted spectral contributions.

are close to that of the doublet contribution of G[Zn5] at RT spectrum (0.85 mm s^{-1}). These results can be attributed to the two NPs phases observed with TEM differing in Zn-for-Fe substitution, one still superparamagnetic (the fine NPs fraction) and one already magnetically ordered (the elongated rods) at 120 K. At 4.2 K the spectrum consists of a broadened sextet, which was analyzed with two contributions. A main spectral contribution (75%) was assigned to the magnetically ordered goethite-like phase observed at 120 K. The H_f = 50.0 T is smaller than that of bulk goethite (50.6 T). The smaller contribution (25%) has the QS = - 0.26 mm s^{-1} in good agreement with that of bulk goethite (similarly to what observed at RT), and the H_f = 48.2 T, also smaller than that of bulk goethite. This contribution was assigned to the fine NPs fraction observed with TEM, identified as a low-to-null Zn-doped goethite phase (see section S.4 in S. I.), which also became magnetically ordered with the decrease in temperature. Hence, both fractions observed with TEM consist of goethite, as the (broadened and noisier) XRD pattern suggested, but with different properties.

The G[Zn20] spectra, obtained at RT, 120 K and 4.2 K, display similar features to that of G[Zn10], passing from a (super)paramagnetic state at RT, to a magnetically ordered state at 4.2 K, with similar hyperfine parameters for the spectral contributions at RT and 120 K. At 120 K, a smaller and less intense sextet is visible, with a mean H_f = 36.5 T lower than that of G[Zn10] (H_f = 44.5 T). The 4.2 K spectrum displays a sextet with broad peaks, especially for line 6 (far right peak), which suggests the presence of at least two different phases, now all magnetically ordered, and has been fit with three spectral contributions. The red sextet (65%), with an IS = 0.33 mm s^{-1} and a QS = −0.14 mm s^{-1}, and a mean H_f = 48.7 T, suggests the presence of a Zn-doped goethite-like phase. The significant spectral contributions of the goethite phase most likely accounts for both the elongated fine rods and a consistent (if not the whole) fraction of fine NPs observed with TEM, similarly to what was observed for G[Zn10]. The ultrafine nature of such goethite-like NPs, corroborated by the very low T_N, explains why this phase was not visible in the XRD pattern. The intermediate cyan sextet (31%) has QS = 0.00 mm s^{-1}, typical of spinel-like structures, and H_f = 50.6 T. These suggest the presence of a non-stoichiometric zinc ferrite phase (known for having T_N < 10 K), in agreement with the XRD results and literature [103–109]. This phase could belong to a fraction of the fine and/or small spherical NPs observed with TEM, in agreement with the FE-SEM observations by Krehula et al., 2006 [82]. Finally, the blue sextet (13%) has QS = 0.06 mm s^{-1}, again close to zero, with a high H_f = 52.3 T, suggesting the presence of a low-to-null Zn-substituted maghemite phase. This probably belongs to a fraction of the fine NPs observed with TEM, as no contribution from this phase was observed at higher temperatures (superparamagnetism) and with XRD.

To summarize TEM, SAED, XRD and MS results: G consisted of rod-shaped NPs of pure polycrystalline goethite dispersed in size; G[Zn5] consisted of elongated rod-shaped NPS of homogeneously 5%at. Zn-

Table 4
MS reference values and fitting parameters of G, G[Zn5], G[Zn10] and G[Zn20] at 300 K, 120 K and 4.2 K.

Sample	*T (K)*	*IS (mm·s^{-1})*	*QS (mm·s^{-1})*	*H_f (T)*	*Γ (mm·s^{-1})*	*Phase*	*Spectral contribution (%)*
Bulk goethite reference values [99]	300	0.37	-0.26	38.0	-	-	-
	4.2	0.37	-0.25	50.6	-	-	-
G	300	0.38	-0.26	32.4*	0.28	α-FeOOH	100
	120	0.36	-0.24	48.9*	0.26	α-FeOOH	100
G[Zn5]	300	0.38	-0.24	24.6*	0.53	α-(Zn,Fe)OOH Fe^{3+}	77
		0.42	0.85ˆ	-	0.85		23
	4.2	0.35	-0.21	49.6*	0.32	α-(Zn,Fe)OOH	100
G[Zn10]	300	0.35	0.81	-	0.40	Fe^{3+}	24
		0.38	0.48	-	0.34	Fe^{3+}	37
		0.65	-	-	4.67	Fe^{3+}	39
	120	0.33	0.85	-	0.65	Fe^{3+}	5
		0.36	-0.21	44.5*	0.28	α-(Zn,Fe)OOH Fe^{3+}	64
		0.35	-	-	6.32		31
	4.2	0.35	-0.20	50.0	0.39	α-(Zn,Fe)OOH α-(Zn,Fe)OOH	75
		0.35	-0.26	48.2	0.44		25
G[Zn20]	300	0.33	0.76	-	0.43	Fe^{3+}	35
		0.35	0.44	-	0.36	Fe^{3+}	28
		0.28	-0.26	36.1*	0.30	Fe^{3+}	37
	120	0.32	0.79	-	0.67	Fe^{3+}	16
		0.36	-0.19	36.5*	0.26	α-(Zn,Fe)OOH Fe^{3+}	29
		0.35	-	-	2.29		55
	4.2	0.34	0.06	52.3	0.34	γ-Fe_2O_3	13
		0.34	0.00	50.6	0.47	$ZnFe_2O_4$	31
		0.33	-0.14	48.7*	0.41	α-(Zn,Fe)OOH	56

Experimental uncertainties: I.S. ± 0.01 mm s^{-1}; Q.S. ± 0.01 mm s^{-1}; Γ ± 0.01 mm s^{-1}; H_f ± 0.1 T; Spectral contribution: ± 3%. *Average magnetic field. ˆFixed value.

doped polycrystalline goethite dispersed in size; G[Zn10] consisted of two goethite-like phases, one of fine elongated rods with a certain degree of Zn-for-Fe substitution (75%), and one of fine NPs with low-to-null Zn-for-Fe substitution (25%); G[Zn20] consisted of two Zn-doped goethite-like structures, consisting of a few extremely fine elongated rods and a consistent amount of fine NPs (56%), a relatively consistent fraction of non-stoichiometric zinc ferrite NPs (31%), and a small fraction of fine maghemite NPs (13%).

3.2.1. Point of zero charge

The polynomial and linear interpolations of the calculated ΔpH against pH_{in} for all samples are shown in Section S.5, and the results are shown in Fig. 4.

The fact that G[Zn5] displays the highest point of zero charge implies that its surface is "more positive" in the pH range of interest, i.e., pH 6–8. This should translate in a surface with higher surface sites density and hence higher adsorption performances (surface-wise) compared to the other samples. It seems surprising that substituting Fe^{3+} in goethite with Zn^{2+}, which has a lower preferential oxidation state and a lower Pauling's electronegativity (1.5) compared to Fe (1.8) [110], promotes an overall higher surface charge. Two possible effects might explain this unexpected observation. The first is based on Giovanoli et al., 1992 [63], who proposed that the charge imbalance due to Zn-for-Fe substitution in goethite is compensated by protonation of the Zn site. This might result in an overall higher protonation of the goethite NPs surface in water. The second is based on the observed elongation of the NPs, which may lead to different availability of crystal faces with higher density of higher active adsorption sites, resulting in a more effective surface for adsorption. A combination of the two effects is not to be excluded, since sample G[Zn10], which has higher Zn content, should also have higher protonation, but has a lower pzc. Further experiments on surface protonation and adsorption sites density are recommended to identify the dominating effect.

Table 5
pzc values of the synthesized NPs obtained from the polynomial and the linear data interpolation approaches.

Sample	*pzc (polynomial)*	*pzc (linear)*
G	8.42	8.42
G[Zn5]	8.81	8.81
G[Zn10]	8.48	8.56
G[Zn20]	8.10	8.12

An excess error of ± 0.15 is assigned to all the pzc values.

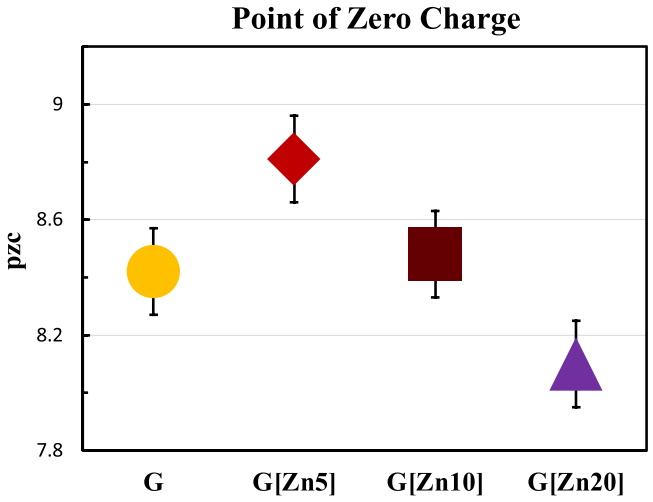

Fig. 4. pzc values estimated from the polynomial data interpolation.

3.3. Adsorption equilibrium

Fig. 5 shows the mass normalized adsorption isotherms, which fitting parameters values are reported in Table 6.

P adsorption is increasing with increased doping, and the respective q_{max} and K_F values confirm this trend. In the case of G[Zn10] and G[Zn20], this is explained by the higher SSA available, due to the fine NPs fraction. The affinities, K_L, follow the trend: G[Zn5] ≳ G >> G[Zn20] ≳ G[Zn10] (Fig. 6) which suggests that G and G[Zn5] being more efficient in adsorbing P even at low concentrations, compared to G[Zn10] and G[Zn20]. As previously stated, affinity is a key factor when targeting

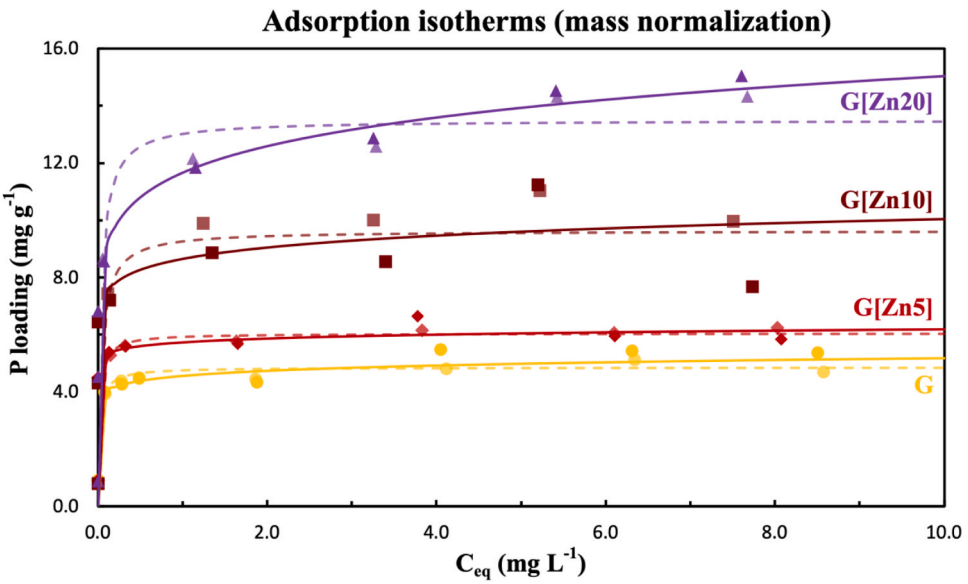

Fig. 5. Freundlich (solid line) and Langmuir (dashed line) adsorption isotherms with the duplicates data of the different synthesized NPs. Results are normalized with respect to the mass of adsorbent.

Table 6
Langmuir and Freundlich fitting parameter of G, G[Zn5], G[Zn10] and G[Zn20] adsorption isotherms normalized to the mass of the adsorbent, with the relative RMSPE.

Sample	*Langmuir*			*Freundlich*		
	q_{max} [mg g^{-1}]	K_L [L mg^{-1}]	*RMSPE*	n	K_F [(mg g^{-1})(mg L^{-1})$^{-n}$]	RMSPE
G	5	47	0.34	0.06	5	0.34
G[Zn5]	6	49	0.47	0.03	6	0.47
G[Zn10]	10	25	0.58	0.07	9	0.58
G[Zn20]	14	27	0.58	0.10	12	0.58

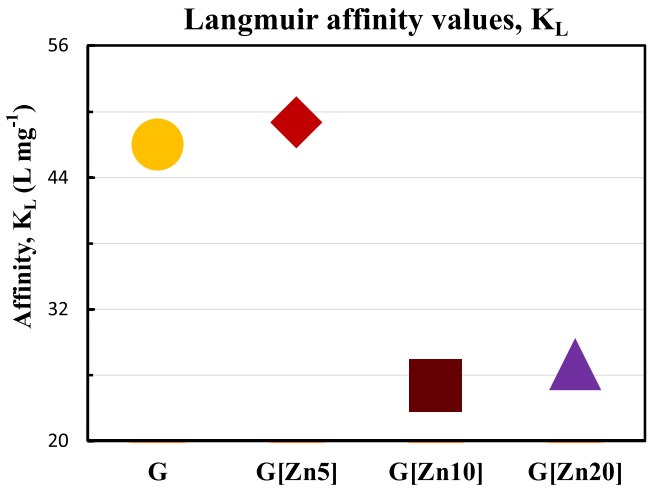

Fig. 6. Affinity values, K_L, retrieved from the adsorption isotherm analysis for each sample.

removal at (ultra-)low concentrations [23]. This shows that Zn-doping of goethite preserves (perhaps improves, but further research is needed) its high affinity, while improving P adsorption (~ 33% higher P loading), most likely due to surface protonation and/or specific crystal faces growth, as discussed for the pzc.

Discussing more in detail the fitting results for each sample, it is possible to observe that for both G and G[Zn5], both models seem to describe the adsorption trend well. In the case of the Langmuir model, which is based on homogeneous monolayer-like adsorption, this could be explained with the more homogeneous particles' shape of the two samples, as well as a general low initial P concentration at which the experiments have been run. For G[Zn10] it is not clear whether a multistep adsorption mechanism is taking place (i.e., multilayer and/or multiple sites adsorption), given the two different NPs phases in G[Zn10], and both isotherms appear to reasonably describe the adsorption trend. For G[Zn20], either a multistep adsorption or a (heterogeneous) Freundlich-like adsorption trend is visible, as expected by the presence of multiple NPs phases, and the Langmuir model is clearly inadequate to describe the data.

No clear trend could be identified from the Freundlich parameter n. These results suggest that the higher P removal performances of G[Zn10] and G[Zn20] are due to the higher SSA, which offer higher capacity, while G and G[Zn5] showed higher affinity for P, but lower capacity.

It is important to keep in mind the limitations and intended use of the Langmuir and the Freundlich models discussed in Section 2.7.

The adsorption isotherm results have also been normalized per SSA, which provides an indication of the adsorbed P surface density, to identify the sample with the "most effective" surface for P adsorption. Fig. 7 shows the resulting graph and the fitting parameters values are reported in Table 7, and it is possible to appreciate the differences between this case and that of Fig. 5. Here, all the isotherms collapsed within the same range of G, except for G[Zn5], which appeared to outperform the others. This further suggest that G[Zn5] surface is more effective in P adsorption, supporting the hypotheses about protonation and functional crystal faces growth. Namely, the surface protonation might exert an additional driving force on phosphate, attracting more of it to the NPs surface (higher affinity). Then, phosphate is adsorbed to the

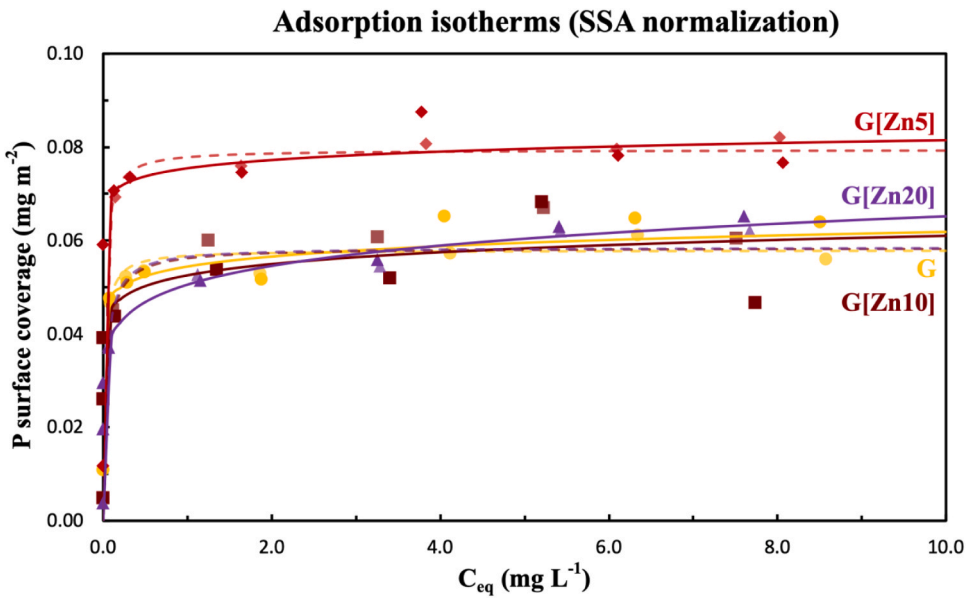

Fig. 7. Freundlich (solid line) and Langmuir (dashed line) adsorption isotherms with the duplicate data of the different synthesized NPs. Results are normalized with respect to the SSA of adsorbent.

Table 7
Langmuir and Freundlich fitting parameter of G, G[Zn5], G[Zn10] and G[Zn20] adsorption isotherms normalized to the SSA of the adsorbent, with the relative RMSPE.

Sample	*Langmuir*			*Freundlich*		
	q_{max} [mg m^{-2}]	K_L [L mg^{-1}]	*RMSPE*	n	K_F [(mg m^{-2})(mg L^{-1})$^{-n}$]	RMSPE
G	0.06	47	0.34	0.06	0.05	0.34
G[Zn5]	0.08	49	0.47	0.03	0.07	0.47
G[Zn10]	0.06	25	0.58	0.07	0.05	0.58
G[Zn20]	0.06	27	0.58	0.11	0.05	0.58

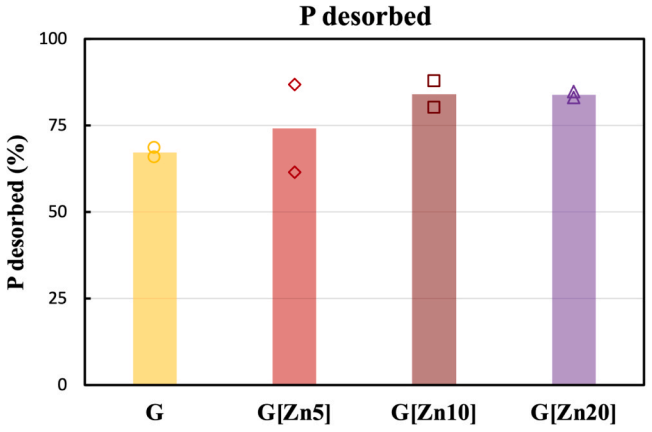

Fig. 8. Percentage of P desorbed after pH increase to 12.6.

crystal faces with high adsorption sites density promoted by the increased NPs aspect ratio (higher capacity per SSA). Also, these results show that a small fraction of the large SSA of G[Zn10] and G[Zn20] is effectively involved in P adsorption, meaning that they have a less functional surface for P adsorption. In fact, compared to G[Zn5], G [Zn10] and G[Zn20] display more than two and three times higher SSA, respectively, but their adsorption capacities are less than two and three times higher, respectively.

Table 8
Desorbed P and relative surface hindrance of undesorbed P of samples G, G [Zn5], G[Zn10] and G[Zn20].

Sample	P desorbed % w/w	% SSA still covered
G	65 ± 1	6.8 ± 0.7
G[Zn5]	71 ± 12	8 ± 4
G[Zn10]	80 ± 4	3.7 ± 0.9
G[Zn20]	80 ± 1	4.0 ± 0.2

3.4. Regeneration test

The adsorption experiment performed prior the regeneration test showed the same trend observed for the adsorption isotherms experiments in Fig. 5 and Fig. 7, and the results are reported in Figure S5 and Table S1.

Note that the desorption experiments were performed at a lower pH (12.6), compared to the usual pH of 13–14 found in literature [23–25, 36,37,55,93]. This was deliberately done to enhance any observable differences in the desorption behaviors. Fig. 8 reports the desorbed P percentages for each sample, calculated as the mg P desorbed over the mg P adsorbed. Table 8 reports these values, with the SSA coverage percentage of the undesorbed P. The desorption results show that, on average, P desorption increased with increasing doping, or at least it was in the same order of magnitude of that of pure G, following a trend: G [Zn20] $\gtrsim$ G[Zn10] > G[Zn5] $\gtrsim$ G. For samples G[Zn10] and G[Zn20], this suggests that P is more loosely bound, probably physisorbed, and it can be speculated that this is due to the fine NPs fraction. The undesorbed fraction caused a surface coverage from a minimum of 3.7(9) % for G[Zn10], to a maximum value of 8(4) % for G[Zn5]. These results

show the high recovery potential of P for the doped samples, already at a pH of 12.6, which means that Zn-doping did not affect the P binding mechanism, such as creating stronger bonds, other complexes or phases (surface precipitates), which would require other regeneration steps, such as acid washes (to remove surface precipitates). Further investigation on the P recovery potential and long term regenerability of the NPs, especially at higher pH, is needed, preferably after embedding them onto a support.

3.5. MS analysis of regenerated samples

After the adsorption-desorption cycle, all samples have been analyzed with Mössbauer spectroscopy, to inspect the stability and any possible change in the structure and phase of the NPs, related to the whole process. However, spectral changes are expected as a result of crystallite growth, fine NPs loss, improved crystallinity (NaOH exposure) and phase transformation during sample preparation. All graphs are shown in figure S4 and the fitting parameters' values are reported in Table S1.

Sample G did not show any appreciable difference from that of the fresh sample, and the analysis confirmed that the sample remained stable.

Conversely, the spectrum of G[Zn5] at RT does display some differences, showing a better definition of the sextet with a slight increase in the mean $H_f = 25.6$ T (24.6 T in the fresh sample). However, the spectrum at 120 K is in good agreement to that of the fresh sample, suggesting that the differences observed at RT are probably related to the sample preparation effects, such as crystallite growth. An effect linked to the undesorbed P could be excluded, as the residual fraction on the surface is negligible, and it anyway should further reduce the H_f [111], rather than increase it. No dissolved Zn and Fe was observed with ICP analysis, suggesting that G[Zn5] remained stable throughout the process.

The MS spectra of G[Zn10] display similar features to that of the fresh sample, also with better defined peaks, and differences in the spectral contributions. This suggests that some of the fine NPs contributing to the significant superparamagnetic relaxation features observed in the fresh samples went through crystallite growth and/or went lost during sample manipulation.

Finally, the MS spectra of G[Zn20], similarly to G[Zn10], displays better defined peaks and differences in spectral contributions. In particular, the 4.2 K measurement still consists of three contributions, but the observed differences suggest that recrystallization might have happened throughout the process. In fact, the maghemite-like phase, shows an increase in H_f value from 52.3 T to 52.9 T, as a result of improved crystallinity. Similarly, the zinc ferrite phase displayed improved crystallinity as the H_f increased from 50. 6 T to 51.5 T, as well as the Zn-doped goethite, which mean H_f increased from 48.7 T to 49.3 T. However, a consistent relative reduction in the maghemite-like and zinc ferrite phases, and a consequent increase in that of Zn-doped goethite, suggests that either a fraction of the maghemite and zinc ferrite NPs recrystallized into goethite or went lost during sample manipulation.

To summarize, throughout the adsorption-desorption cycle, G and G[Zn5] appeared to remain stable, as no significant phase changes have been observed in the Mössbauer analysis of the regenerated samples. G[Zn10] displayed slight changes, due to improved crystallinity or fine NPs loss. Differently, G[Zn20] displayed consistent differences, due to either consistent dissolution/recrystallization of zinc ferrite NPs and/or fine NPs loss.

4. Towards an effective, stable and regenerable P adsorbent

The experimental results show that 5%at. was the best Zn-doping percentage for goethite to boost its P recovery performances. First, the NPs phase and morphology were preserved up to 5%at. doping, as TEM, XRD and MS measurements proved them to consist of Zn-doped goethite rods, with increased aspect ratio. This Zn-doping percentage led to an increase in the (positive) surface charge, testified by the highest pzc. Regarding P adsorption, sample G[Zn5] was able to remove about 25% more P per mass of adsorbent compared to the pure goethite phase. Even though G[Zn10] and G[Zn20] had SSA two and three times higher than that of G[Zn5], respectively, the P removal performances for them did not increase accordingly (50% and 100% more, respectively). Moreover, the G[Zn5] also displayed the highest affinity for P, which is the key parameter to assess how good the adsorbent is in removing P, even at ultra-low P concentrations, and the highest P removal per SSA. These results support the idea of the higher surface protonation and growth of crystal faces with higher active sites density in Zn-doped goethite. Further research on adsorption site distribution and phosphate bond, for instance with FTIR, would help confirming these interpretations, while improving the understanding of the iron oxide-phosphate binding mechanism. Furthermore, P desorption was not compromised but on average improved with Zn-doping, meaning that the P binding mechanism was not affected, and suggesting an improved P recovery potential. In addition, G and G[Zn5] appeared to remain stable throughout the whole adsorption/desorption process, better sustaining the different environmental conditions compared to G[Zn10] and G[Zn20]. Further research is needed to identify the optimum Zn-doping percentage, by investigating other intermediate percentages between 0 % and 5 %at. and 5–10 %at., to better understand the trend of the improved properties. Also, to fully assess the adsorption performances and the stability of the adsorbent in the long term, multiple adsorption/desorption experiments in real water, with regenerations performed at higher pH, are highly recommended. In fact, it has been suggested that to properly assess the selectivity of the adsorbent, tests should be performed in real water, where different anions, cations, and organics are coexisting, rather than in synthetic solution with only one or few competing anions [23]. In our case, to do so, considering that applying bare nanoparticles in water treatment is challenging, we recommend embedding such nanoparticles onto a support, like for the case of HAIX.

5. Conclusions

This study showed that Zn-doping of goethite NPs improves the properties for P removal at ultra-low concentrations of goethite, while preserving its stability and the P recovery potential. The higher P adsorption was linked to the higher pzc and the higher affinity of Zn-doped goethite for P, the latter being a key factor when targeting the ultra-low P concentrations. This highlights the importance of developing adsorbents with more effective and functional surfaces for P adsorption, rather than adsorbents with only higher SSA.

These results set the basis for developing a regenerable and stable, thus long lasting, goethite-based adsorbent with enhanced P recovery potential. Embedding such developed NPs on a support (e.g., HAIX), would bring them to real-life application, improve the adsorbent reusability and make the process economically viable. Further research on adsorbent Zn-doping optimization, NPs support and long-term reusability with real-life conditions would be highly recommended.

CRediT authorship contribution statement

A.I. Dugulan: Conceptualization, Methodology, Project administration, Supervision, Writing – original draft, Writing – review & editing. **E. Brück:** Conceptualization, Methodology, Project administration, Supervision, Writing – original draft, Writing – review & editing. **G.J. Witkamp:** Conceptualization, Methodology, Supervision, Writing – original draft, Writing – review & editing. **L. Korving:** Conceptualization, Funding acquisition, Methodology, Supervision, Writing – original draft, Writing – review & editing. **C. Belloni:** Conceptualization, Data curation, Formal analysis, Investigation, Methodology, Writing – original draft, Writing – review & editing.

Declaration of Competing Interest

The authors declare the following financial interests/personal relationships which may be considered as potential competing interests. Carlo Belloni reports financial support was provided by Netherlands Organization for Scientific Research.

Data Availability

Data will be made available on request.

Acknowledgments

This work was performed in the cooperation framework of Wetsus, European Centre of Excellence for Sustainable Water Technology (www.wetsus.nl). Wetsus is co-funded by the Dutch Ministry of Economic Affairs and Ministry of Infrastructure and Environment, the European Union Regional Development Fund, the Province of Fryslân and the Northern Netherlands Provinces. This research received funding from the Netherlands Organization for Scientific Research (NWO, award number 731.017.406) in the framework of the Innovation Fund for Chemistry, and from the Ministry of Economic Affairs and Climate Policy in the framework of the TKI/PPS-Toeslagregeling. The authors thank the participants of the research theme "Phosphate recovery" for the interest, fruitful discussions, and financial support (Aquacare, Kemira, Waterschapsbedrijf Limburg, Waterschap Brabantse Delta, Aqua Minerals, VCS Denmark, Royal HaskoningDHV). A special thanks goes to Pim de Jager and Raimonda Buliauskaitė (Aquacare) for the frequent knowledge exchange and interest in the research, Harm van der Kooi and the Wetsus Analytical Team for the technical support, Michel Steenvoorden and Maxim Ariens for the support with Mössbauer spectroscopy related matters, Kees Goubitz (TU Delft) for the support on XRD, Wiel Evers (TU Delft) for the TEM measurements, Jouk Jansen (TU Delft) for the support with SAED analysis, Renata van der Weijden (WUR) for the fruitful discussions, Prashanth Suresh Kumar (Plaksha University) and Terica Sinclair for the support and guidance, Amandine Dronne, Varad Kapur, Maddalena Tigli for the work done together.

Appendix A. Supporting information

Supplementary data associated with this article can be found in the online version at doi:10.1016/j.colsurfa.2024.133476.

References

[1] USEPA, (2015).
[2] D.P. Van Vuuren, A.F. Bouwman, A.H.W. Beusen, Phosphorus demand for the 1970-2100 period: a scenario analysis of resource depletion, Glob. Environ. Chang. 20 (2010) 428–439, https://doi.org/10.1016/j.gloenvcha.2010.04.004.
[3] D. Cordell, J.O. Drangert, S. White, The story of phosphorus: global food security and food for thought, Glob. Environ. Chang. 19 (2009) 292–305, https://doi.org/10.1016/J.GLOENVCHA.2008.10.009.
[4] W.J. Brownlie, M.A. Sutton, D. Cordell, D.S. Reay, K.V. Heal, P.J.A. Withers, I. Vanderbeck, B.M. Spears, Phosphorus price spikes: a wake-up call for phosphorus resilience, Front. Sustain. Food Syst. 7 (2023), https://doi.org/10.3389/fsufs.2023.1088776.
[5] J.J. Schröder, D. Cordell, A.L. Smit, A. Rosemarin, Sustainable use of phosphorus Report 357 (European Union tender project ENV.B.1/ETU/2009/0025), (2009) 140. ⟨http://ec.europa.eu/environment/natres/pdf/phosphorus/sustainable_use_phosphorus.pdf⟩.
[6] A.L. Smit, P.S. Bindraban, J.J. Shroeder, J.G. Conijin, H.G. van der Meer, Phosphorus in agriculture: global resoources, trends and developments: report to the Steering Committee Technology Assessment of the Ministery of Agriculture, Nature and Food Quality, The Netherlands, and in collaboration with the Nutrient Flow Task Group, Plant Res. Int 282 (2009) 36. ⟨http://77.245.87.41/Portals/0/duurzaamheid/biobrandstoffen/nieuws/2009/11/12571.pdf⟩.
[7] USGS, Mineral commodity summaries 2020, 2020. ⟨https://pubs.usgs.gov/periodicals/mcs2020/mcs2020.pdf⟩.
[8] EC, Critical Raw Materials, 2020. ⟨https://doi.org/10.1007/978-3-030-40268-6_9⟩.
[9] EC, European Green Deal, 2020. ⟨https://doi.org/10.4324/9780080495781-12⟩.
[10] EC, Circular Economy Action Plan, 2020. ⟨https://doi.org/10.7312/columbia/9780231167352.003.0015⟩.
[11] D.L. Correll, The role of phosphorus in the eutrophication of receiving waters: a review, J. Environ. Qual. 27 (1998) 261–266, https://doi.org/10.2134/jeq1998.00472425002700020004x.
[12] D.W. Schindler, Eutrophication and recovery in experimental lakes: iImplications for lake management, Science 184 (80) (1974) 897–899, https://doi.org/10.1126/science.184.4139.897.
[13] D.W. Schindler, Whole-lake eutrophication experiments with phosphorus, nitrogen and carbon, SIL Proc., 1922-2010 19 (1975) 3221–3231, https://doi.org/10.1080/03680770.1974.11896436.
[14] D.W. Schindler, Evolution of phosphorus limitation in lakes, Science 195 (80) (1977) 260–262, https://doi.org/10.1126/science.195.4275.260.
[15] D.W. Schindler, S.R. Carpenter, S.C. Chapra, R.E. Hecky, D.M. Orihel, Reducing phosphorus to curb lake eutrophication is a success, Environ. Sci. Technol. 50 (2016) 8923–8929, https://doi.org/10.1021/acs.est.6b02204.
[16] J.N. Pretty, C.F. Mason, D.B. Nedwell, R.E. Hine, S. Leaf, R. Dils, Environmental costs of freshwater eutrophication in England and Wales, Environ. Sci. Technol. 37 (2003) 201–208, https://doi.org/10.1021/es020793k.
[17] S.R. Carpenter, Phosphorus control is critical to mitigating eutrophication, Proc. Natl. Acad. Sci. U. S. A. 105 (2008) 11039–11040, https://doi.org/10.1073/pnas.0806112105.
[18] W.K. Dodds, W.W. Bouska, J.L. Eitzmann, T.J. Pilger, K.L. Pitts, A.J. Riley, J. T. Schloesser, D.J. Thornbrugh, Eutrophication of U. S. freshwaters: analysis of potential economic damages, Environ. Sci. Technol. 43 (2009) 12–19, https://doi.org/10.1021/es801217q.
[19] I. Chorus, I.R. Falconer, H.J. Salas, J. Bartram, Health risks caused by freshwater cyanobacteria in recreational waters, J. Toxicol. Environ. Heal. - Part B Crit. Rev. 3 (2000) 323–347, https://doi.org/10.1080/109374000436364.
[20] L. Carvalho, C. Mcdonald, C. De Hoyos, U. Mischke, G. Phillips, G. Abor Borics, S. Poikane, B. Skjelbred, A.L. Solheim, J. Van Wichelen, A.C. Cardoso, Sustaining recreational quality of European lakes: minimizing the health risks from algal blooms through phosphorus control On secondment from CEH 2 to JRC 1, J. Appl. Ecol. 50 (2013) 315–323, https://doi.org/10.1111/1365-2664.12059.
[21] EC, The urban waste water treatment directive, 1992.
[22] EEA, European waters Assessment of status and pressures 2018, 2018.
[23] P.S. Kumar, L. Korving, M.C.M. van Loosdrecht, G.J. Witkamp, Adsorption as a technology to achieve ultra-low concentrations of phosphate: research gaps and economic analysis, Water Res. X. 4 (2019) 100029, https://doi.org/10.1016/J.WROA.2019.100029.
[24] P. Suresh Kumar, W.W. Ejerssa, C.C. Wegener, L. Korving, A.I. Dugulan, H. Temmink, M.C.M. van Loosdrecht, G.J. Witkamp, Understanding and improving the reusability of phosphate adsorbents for wastewater effluent polishing, Water Res 145 (2018) 365–374, https://doi.org/10.1016/j.watres.2018.08.040.
[25] P. Loganathan, S. Vigneswaran, J. Kandasamy, N.S. Bolan, Removal and recovery of phosphate from water using sorption, Crit. Rev. Environ. Sci. Technol. 44 (2014) 847–907, https://doi.org/10.1080/10643389.2012.741311.
[26] T.A.H. Nguyen, H.H. Ngo, W.S. Guo, J. Zhang, S. Liang, D.J. Lee, P.D. Nguyen, X. T. Bui, Modification of agricultural waste/by-products for enhanced phosphate removal and recovery: potential and obstacles, Bioresour. Technol. 169 (2014) 750–762, https://doi.org/10.1016/j.biortech.2014.07.047.
[27] W. Huang, X. Yu, J. Tang, Y. Zhu, Y. Zhang, D. Li, Enhanced adsorption of phosphate by flower-like mesoporous silica spheres loaded with lanthanum, Microporous Mesoporous Mater. 217 (2015) 225–232, https://doi.org/10.1016/j.micromeso.2015.06.031.
[28] K.Y. Koh, S. Zhang, J. Paul Chen, Hydrothermally synthesized lanthanum carbonate nanorod for adsorption of phosphorus: material synthesis and optimization, and demonstration of excellent performance, Chem. Eng. J. 380 (2020) 122153, https://doi.org/10.1016/j.cej.2019.122153.
[29] W. Gu, X. Li, M. Xing, W. Fang, D. Wu, Removal of phosphate from water by amine-functionalized copper ferrite chelated with La(III), Sci. Total Environ. 619–620 (2018) 42–48, https://doi.org/10.1016/j.scitotenv.2017.11.098.
[30] P.S. Kumar, L. Korving, M.C.M. van Loosdrecht, G.J. Witkamp, Adsorption as a technology to achieve ultra-low concentrations of phosphate: research gaps and economic analysis, Water Res. X. 4 (2019) 100029, https://doi.org/10.1016/j.wroa.2019.100029.
[31] X. Huang, S. Guida, B. Jefferson, A. Soares, Economic evaluation of ion-exchange processes for nutrient removal and recovery from municipal wastewater, Npj Clean. Water 3 (2020), https://doi.org/10.1038/s41545-020-0054-x.
[32] R.M. Cornell, U. Schwertmann, Iron Oxides (2003), https://doi.org/10.1002/3527602097.
[33] S. Guida, G. Rubertelli, B. Jefferson, A. Soares, Demonstration of ion exchange technology for phosphorus removal and recovery from municipal wastewater, Chem. Eng. J. 420 (2021) 129913, https://doi.org/10.1016/j.cej.2021.129913.
[34] H. Bacelo, A.M.A. Pintor, S.C.R. Santos, R.A.R. Boaventura, C.M.S. Botelho, Performance and prospects of different adsorbents for phosphorus uptake and recovery from water, Chem. Eng. J. 381 (2020) 122566, https://doi.org/10.1016/j.cej.2019.122566.
[35] D. Pinelli, S. Bovina, G. Rubertelli, A. Martinelli, S. Guida, A. Soares, D. Frascari, Regeneration and modelling of a phosphorous removal and recovery hybrid ion exchange resin after long term operation with municipal wastewater, Chemosphere 286 (2022) 131581, https://doi.org/10.1016/j.chemosphere.2021.131581.
[36] A. Genz, A. Kornmüller, M. Jekel, Advanced phosphorus removal from membrane filtrates by adsorption on activated aluminium oxide and granulated ferric

hydroxide, Water Res 38 (2004) 3523–3530, https://doi.org/10.1016/j.watres.2004.06.006.
[37] L.M. Blaney, S. Cinar, A.K. SenGupta, Hybrid anion exchanger for trace phosphate removal from water and wastewater, Water Res 41 (2007) 1603–1613, https://doi.org/10.1016/j.watres.2007.01.008.
[38] U. Schwertmann, E. Murad, Effect of pH on the formation of goethite and hematite from ferrihydrite, Clays Clay Min. 31 (1983) 277–284, https://doi.org/10.1346/CCMN.1983.0310405.
[39] M. Villacis-Garcia, M. Ugalde-Arzate, K. Vaca-Escobar, M. Villalobos, R. Zanella, N. Martinez-Villegas, Laboratory synthesis of geothite ad ferrihydrite of controlled partocel sozes, Bol. La Soc. Geol. Mex. 67 (2015) 433–446.
[40] J. Antelo, M. Avena, S. Fiol, R. López, F. Arce, Effects of pH and ionic strength on the adsorption of phosphate and arsenate at the goethite-water interface, J. Colloid Interface Sci. 285 (2005) 476–486, https://doi.org/10.1016/j.jcis.2004.12.032.
[41] R.J. Atkinson, A.M. Posner, J.P. Quirk, Adsorption of potential-determining ions at ferric-aqueous electrolyte interface, J. Phys. Chem. 71 (1967) 550.
[42] R.P.J.J. Rietra, T. Hiemstra, W.H. Van Riemsdijk, Interaction between calcium and phosphate adsorption on goethite, Environ. Sci. Technol. 35 (2001) 3369–3374, https://doi.org/10.1021/es000210b.
[43] R.L. Parfitt, R.J. Atkinson, Phosphate adsorption on goethite (α-FeOOOH), Nature 264 (1976) 740–742, https://doi.org/10.1038/264740a0.
[44] R. Chitrakar, S. Tezuka, A. Sonoda, K. Sakane, K. Ooi, T. Hirotsu, Phosphate adsorption on synthetic goethite and akaganeite, J. Colloid Interface Sci. 298 (2006) 602–608, https://doi.org/10.1016/j.jcis.2005.12.054.
[45] J. Torrent, V. Barrón, U. Schwertmann, Phosphate adsorption and desorption by goethites differing in crystal morphology, Soil Sci. Soc. Am. J. 54 (1990) 1007–1012, https://doi.org/10.2136/sssaj1990.03615995005400040012x.
[46] S.H. Lin, H.C. Kao, C.H. Cheng, R.S. Juang, An EXFAS study of the structures of copper and phosphate sorbed onto goethite, Colloids Surf. A Physicochem. Eng. Asp. 234 (2004) 71–75, https://doi.org/10.1016/j.colsurfa.2003.12.005.
[47] X. Wang, F. Liu, W. Tan, W. Li, X. Feng, D.L. Sparks, Characteristics of phosphate adsorption-desorption onto ferrihydrite: comparison with well-crystalline fe (Hydr)oxides, Soil Sci. 178 (2013) 1–11, https://doi.org/10.1097/SS.0b013e31828683f8.
[48] F.A. Ponce, D.P. Bour, Nitride-based semiconductors for blue and green light-emitting devices, Nature 386 (1997) 351–359, https://doi.org/10.1038/386351a0.
[49] K. Sivula, R. Van De Krol, Semiconducting materials for photoelectrochemical energy conversion, Nat. Rev. Mater. 1 (2016), https://doi.org/10.1038/natrevmats.2015.10.
[50] K. Zhang, J. Robinson, Doping of Two-Dimensional Semiconductors: A Rapid Review and Outlook, (2019). ⟨https://doi.org/10.1557/adv.2019.391⟩.
[51] L.F. Liotta, M. Gruttadauria, G. Di Carlo, G. Perrini, V. Librando, Heterogeneous catalytic degradation of phenolic substrates: catalysts activity, J. Hazard. Mater. 162 (2009) 588–606, https://doi.org/10.1016/j.jhazmat.2008.05.115.
[52] D.W. Lee, M.S. Lee, J.Y. Lee, S. Kim, H.J. Eom, D.J. Moon, K.Y. Lee, The review of Cr-free Fe-based catalysts for high-temperature water-gas shift reactions, Catal. Today 210 (2013) 2–9, https://doi.org/10.1016/j.cattod.2012.12.012.
[53] M. Zhu, I.E. Wachs, A perspective on chromium-Free iron oxide-based catalysts for high temperature water-gas shift reaction, Catal. Today 311 (2018) 2–7, https://doi.org/10.1016/j.cattod.2017.08.042.
[54] S. Rahim Pouran, A.A. Abdul Raman, W.M.A. Wan Daud, Review on the application of modified iron oxides as heterogeneous catalysts in Fenton reactions, J. Clean. Prod. 64 (2014) 24–35, https://doi.org/10.1016/j.jclepro.2013.09.013.
[55] M. Li, J. Liu, Y. Xu, G. Qian, Phosphate adsorption on metal oxides and metal hydroxides: a comparative review, Environ. Rev. 24 (2016) 319–332, https://doi.org/10.1139/er-2015-0080.
[56] P.L. Sibrell, G.A. Montgomery, K.L. Ritenour, T.W. Tucker, Removal of phosphorus from agricultural wastewaters using adsorption media prepared from acid mine drainage sludge, Water Res. 43 (2009) 2240–2250, https://doi.org/10.1016/j.watres.2009.02.010.
[57] L. Zhang, Q. Zhou, J. Liu, N. Chang, L. Wan, J. Chen, Phosphate adsorption on lanthanum hydroxide-doped activated carbon fiber, Chem. Eng. J. 185–186 (2012) 160–167, https://doi.org/10.1016/J.CEJ.2012.01.066.
[58] E. Kumar, A. Bhatnagar, W. Hogland, M. Marques, M. Sillanpää, Interaction of inorganic anions with iron-mineral adsorbents in aqueous media - a review, Adv. Colloid Interface Sci. 203 (2014) 11–21, https://doi.org/10.1016/j.cis.2013.10.026.
[59] H. Bacelo, A.M.A. Pintor, S.C.R. Santos, R.A.R. Boaventura, C.M.S. Botelho, Performance and prospects of different adsorbents for phosphorus uptake and recovery from water, Chem. Eng. J. 381 (2020) 122566, https://doi.org/10.1016/j.cej.2019.122566.
[60] E. Murad, J. Cashion, Mössbauer Spectroscopy of Environmental Materials and Their Industrial Utilization, Kluwer Academic Publishers, Dordrecht, 2004.
[61] H. Liu, T. Chen, R.L. Frost, An overview of the role of goethite surfaces in the environment, Chemosphere 103 (2014) 1–11, https://doi.org/10.1016/J.CHEMOSPHERE.2013.11.065.
[62] A. Manceau, M.L. Schlegel, M. Musso, V.A. Sole, C. Gauthier, P.E. Petit, F. Trolard, Crystal chemistry of trace elements in natural and synthetic goethite, Geochim. Cosmochim. Acta 64 (2000) 3643–3661, https://doi.org/10.1016/S0016-7037(00)00427-0.
[63] R. Giovanoli, R.M. Cornell, Crystallization of Metal Substituted Ferrihydrites, Z. F. üR. Pflanz. ährung Und Bodenkd. 155 (1992) 455–460, https://doi.org/10.1002/jpln.19921550517.
[64] P.G. Belelli, S.A. Fuente, N.J. Castellani, Phosphate adsorption on goethite and Al-rich goethite, Comput. Mater. Sci. 85 (2014) 59–66, https://doi.org/10.1016/j.commatsci.2013.12.030.
[65] E. Murad, U. Schwertmann, The influence of aluminium substitution and crystallinity on the Mössbauer spectra of goethite, Clay Min. (1983) 301–312.
[66] D.E. Latta, J.E. Bachman, M.M. Scherer, Fe electron transfer and atom exchange in goethite: influence of Al-substitution and anion sorption, Environ. Sci. Technol. 46 (2012) 10614–10623, https://doi.org/10.1021/es302094a.
[67] H.D. Ruan, R.J. Gilkes, Kinteics of thermal dehydroxylation of aluminous goethite, 1996.
[68] M. Ma, H. Gao, Y. Sun, M. Huang, The adsorption and desorption of Ni(II) on Al substituted goethite, J. Mol. Liq. 201 (2015) 30–35, https://doi.org/10.1016/J.MOLLIQ.2014.11.024.
[69] E. Murad, L.H. Bowen, Magnetic ordering in Al-rich goethites: influence of crystallinity, Am. Mineral. 72 (1987) 194–200.
[70] S.A. Fysh, P.E. Clark, Aluminous goethite: a mössbauer study, Phys. Chem. Miner. 8 (1982) 180–187, https://doi.org/10.1007/BF00308241.
[71] J. Xu, L.K. Koopal, M. Wang, J. Xiong, J. Hou, Y. Li, W. Tan, Phosphate speciation on Al-substituted goethite: ATR-FTIR/2D-COS and CD-MUSIC modeling, Environ. Sci. Nano. 6 (2019) 3625, https://doi.org/10.1039/c9en00539k.
[72] A.C. Scheinost, D.G. Schulze, I. And, U. Schwertmann, Diffuse reflectance spectra of Al substituted goethite: a lingad field approach, 1999.
[73] L.-C. Hsu, Y.-M. Tzou, M.-S. Ho, C. Sivakumar, Y.-L. Cho, W.-H. Li, P.-N. Chiang, H.Y. Teah, Y.-T. Liu, Preferential phosphate sorption and Al substitution on goethite, Environ. Sci. Nano. 7 (2020) 3497, https://doi.org/10.1039/c9en01435g.
[74] D.C. Golden, L.H. Bowen, S.B. Weed, J.M. Bigham, Mössbauer studies of synthetic and soil-occurring aluminum-substituted goethites, Soil Sci. Soc. Am. J. 43 (1979) 802–808, https://doi.org/10.2136/sssaj1979.03615995004300040038x.
[75] J. Torrent, U. Schwertmann, V. Barrón, Fast and slow phosphate sorption by goethite-rich natural materials, Clays Clay Min. 40 (1992) 14–21, https://doi.org/10.1346/CCMN.1992.0400103.
[76] C.C. Ainsworth, M.E. Sumner, Effect of aluminum substitution in goethite on phosphorus adsorption: II. Rate of adsorption, Soil Sci. Soc. Am. J. 49 (1985) 1149–1153, https://doi.org/10.2136/sssaj1985.03615995004900050015x.
[77] W. Stiers, U. Schwertmann, Evidence for manganese substitution in synthetic goethite, Geochim. Cosmochim. Acta 49 (1985) 1909–1911, https://doi.org/10.1016/0016-7037(85)90085-7.
[78] R.E. Vandenberghe, A.E. Verbeeck, E. De Grave, W. Stiers, 57Fe Mössbauer effect study of Mn-substituted goethite and hematite, Hyperfine Inter. 29 (1986) 1157–1160, https://doi.org/10.1007/BF02399440.
[79] K. Rout, A. Dash, M. Mohapatra, S. Anand, Manganese doped goethite: structural, optical and adsorption properties, J. Environ. Chem. Eng. 2 (2014) 434–443, https://doi.org/10.1016/j.jece.2014.01.001.
[80] X. Sun, H.E. Doner, M. Zavarin, Spectroscopy study of arsenite [As(III)] oxidation on Mn-substituted goethite, 1999.
[81] X. Zhang, L. Zhang, Y. Liu, M. Li, X. Wu, T. Jiang, C. Chen, Y. Peng, Mn-substituted goethite for uranium immobilization: a study of adsorption behavior and mechanisms, Environ. Pollut. 262 (2020), https://doi.org/10.1016/j.envpol.2020.114184.
[82] S. Krehula, S. Musić, Ž. Skoko, S. Popović, The influence of Zn-dopant on the precipitation of α-FeOOH in highly alkaline media, J. Alloy. Compd. 420 (2006) 260–268, https://doi.org/10.1016/J.JALLCOM.2005.10.019.
[83] C. Belloni, L. Korving, G.-J. Witkamp, E. Brück, A.I. Dugulan, Effect of goethite doping using elements with different preferential oxidation states for improved reversible phosphate adsorption, Manuscript Submitted for Publication, J. Environ. Chem. Eng. 11 (2023) 110505, https://doi.org/10.1016/j.jece.2023.110505.
[84] C. Belloni, L. Korving, G.J. Witkamp, E. Brück, P. de Jager, A.I. Dugulan, FeOOH and (Fe,Zn)OOH hybrid anion exchange adsorbents for phosphate recovery: a determination of Fe-phases and adsorption–desorption mechanisms, Chem. Eng. J. 473 (2023) 145287, https://doi.org/10.1016/j.cej.2023.145287.
[85] Z. Klencsár, Mössbauer spectrum analysis by evolution algorithm, Nucl. Instrum. Methods Phys. Res. Sect. B Beam Interact. Mater. At. 129 (1997) 527–533, https://doi.org/10.1016/S0168-583X(97)00314-5.
[86] T. Mahmood, M.T. Saddique, A. Naeem, P. Westerhoff, S. Mustafa, A. Alum, Comparison of different methods for the point of zero charge determination of NiO, Ind. Eng. Chem. Res. 50 (2011) 10017–10023, https://doi.org/10.1021/ie200271d.
[87] W.F. Tan, S.J. Lu, F. Liu, X.H. Feng, J.Z. He, L.K. Koopal, Determination of the point-of-zero charge of manganese oxides with different methods including an improved salt titration method, Soil Sci. 173 (2008) 277–286, https://doi.org/10.1097/SS.0b013e31816d1f12.
[88] Y. Mao, A. Ninh Pham, Y. Xin, T. David Waite, Effects of pH, floc age and organic compounds on the removal of phosphate by pre-polymerized hydrous ferric oxides, Sep. Purif. Technol. 91 (2012) 38–45, https://doi.org/10.1016/j.seppur.2011.09.045.
[89] K.J. Powell, P.L. Brown, R.H. Byrne, T. Gajda, G. Hefter, S. Sjöberg, H. Wanner, Chemical speciation of environmentally significant heavy metals with inorganic ligands part 1: the Hg2+- Cl-, OH-, CO32-, so42-, and PO 43- aqueous systems (IUPAC technical report), Pure Appl. Chem. 77 (2005) 739–800, https://doi.org/10.1351/pac200577040739.
[90] V.T. Trinh, T.M.P. Nguyen, H.T. Van, L.P. Hoang, T.V. Nguyen, L.T. Ha, X.H. Vu, T.T. Pham, T.N. Nguyen, N.V. Quang, X.C. Nguyen, Phosphate adsorption by silver nanoparticles-loaded activated carbon derived from tea residue, Sci. Rep. 10 (2020) 1–13, https://doi.org/10.1038/s41598-020-60542-0.

[91] M.K. Ghosh, G.E.J. Poinern, T.B. Issa, P. Singh, Arsenic adsorption on goethite nanoparticles produced through hydrazine sulfate assisted synthesis method, Korean J. Chem. Eng. 29 (2012) 95–102, https://doi.org/10.1007/s11814-011-0137-y.
[92] M. Rashid, N.T. Price, M.Á. Gracia Pinilla, K.E. O'Shea, Effective removal of phosphate from aqueous solution using humic acid coated magnetite nanoparticles, Water Res 123 (2017) 353–360, https://doi.org/10.1016/j.watres.2017.06.085.
[93] A. Drenkova-Tuhtan, M. Schneider, M. Franzreb, C. Meyer, C. Gellermann, G. Sextl, K. Mandel, H. Steinmetz, Pilot-scale removal and recovery of dissolved phosphate from secondary wastewater effluents with reusable ZnFeZr adsorbent @ Fe3O4/SiO2 particles with magnetic harvesting, Water Res 109 (2017) 77–87, https://doi.org/10.1016/J.WATRES.2016.11.039.
[94] G. Zhang, H. Liu, R. Liu, J. Qu, Removal of phosphate from water by a Fe-Mn binary oxide adsorbent, J. Colloid Interface Sci. 335 (2009) 168–174, https://doi.org/10.1016/j.jcis.2009.03.019.
[95] I. Langmuir, The adsorption of gases on plane surfaces of glass, mica and platinum, Res. Lab. Gen. Electr. Co. (1918). ⟨https://pubs.acs.org/sharinggui delines⟩.
[96] H. Freundlich, Über die Adsorption in Lösungen, Z. F. üR. Phys. Chem. (1907).
[97] D.S. Tawfik, R.E. Viola, Arsenate replacing phosphate: alternative life chemistries and ion promiscuity, Biochemistry 50 (2011) 48, https://doi.org/10.1021/bi200002a.
[98] D.M. Smilgies, Scherrer grain-size analysis adapted to grazing-incidence scattering with area detectors, J. Appl. Crystallogr. 42 (2009) 1030–1034, https://doi.org/10.1107/S0021889809040126.
[99] E. Murad, Magnetic properties of microcrystalline iron (III) oxides and related materials as reflected in their Mössbauer spectra, Phys. Chem. Miner. 23 (1996) 248–262, https://doi.org/10.1007/bf00207766.
[100] J.B. Forsyth, C.E. Johnson, P.J. Brown, The magnetic structure and hyperfine field of goethite, Philos. Mag. 10 (1968) 713–721, https://doi.org/10.1080/14786436408228489.
[101] E. de Grave, R.E. Vandenberghe, 57Fe Mössbauer effect study of well-crystallized goethite (α-FeOOH), Hyperfine Inter. 28 (1986) 643–646, https://doi.org/10.1007/BF02061530.
[102] F. van der Woude, J. Dekker, Mossbauer effect in a-FeOOH, 181 (1966).
[103] J.F. Hochepied, P. Bonville, M.P. Pileni, Nonstoichiometric zinc ferrite nanocrystals: syntheses and unusual magnetic properties, J. Phys. Chem. B. 104 (2000) 905–912, https://doi.org/10.1021/jp991626i.
[104] C.N. Chinnasamy, A. Narayanasamy, N. Ponpandian, K. Chattopadhyay, The influence of Fe3 ions at tetrahedral sites on the magnetic properties of nonocrystalline ZnFe2O4, Mater. Sci. Eng. A. 304–306 (2001) 983–987, https://doi.org/10.1016/S0921-5093(00)01611-7.
[105] G.F. Goya, H.R. Rechenberg, M. Chen, W.B. Yelon, Magnetic irreversibility in ultrafine ZnFe2O4 particles, J. Appl. Phys. 87 (2000) 8005–8007, https://doi.org/10.1063/1.373487.
[106] S.J. Stewart, S.J.A. Figueroa, M.B. Sturla, R.B. Scorzelli, F. García, F.G. Requejo, Magnetic ZnFe2O4 nanoferrites studied by X-ray magnetic circular dichroism and Mössbauer spectroscopy, Phys. B Condens. Matter 389 (2007) 155–158, https://doi.org/10.1016/j.physb.2006.07.045.
[107] E.J. Choi, Y. Ahn, K.C. Song, Mössbauer study in zinc ferrite nanoparticles, J. Magn. Magn. Mater. 301 (2006) 171–174, https://doi.org/10.1016/j.jmmm.2005.06.016.
[108] S. Ammar, N. Jouini, F. Fiévet, Z. Beji, L. Smiri, P. Moliné, M. Danot, J. M. Grenèche, Magnetic properties of zinc ferrite nanoparticles synthesized by hydrolysis in a polyol medium, J. Phys. Condens. Matter 18 (2006) 9055–9069, https://doi.org/10.1088/0953-8984/18/39/032.
[109] V. Blanco-Gutiérrez, F. Jiménez-Villacorta, P. Bonville, M.J. Torralvo-Fernandéz, R. Sáez-Puche, Synthesis, characterization and conductivity studies of ZnFe 2 O 4 nanoparticles, J. Phys. Chem. C. (2011) 1627–1634, https://doi.org/10.1063/1.4917792.
[110] W. Gosdy, W.J.Orville Thomas, Electronegativities of the elements, J. Chem. Phys. 24 (1956) 439–444, https://doi.org/10.1063/1.1742493.
[111] J.H. Johnston, K. Norrish, A 57fe mossbauer spectroscopic study of a selection of australian and other goethites, Aust. J. Soil Res 19 (1981) 231–237, https://doi.org/10.1071/SR9810231.